Toward Dual-functional Radar-Communication Systems: Optimal Waveform Design

Fan Liu, *Student Member, IEEE*, Longfei Zhou, *Student Member, IEEE*, Christos Masouros, *Senior Member, IEEE*, Ang Li, *Student Member, IEEE*, Wu Luo, *Member, IEEE*, and Athina Petropulu, *Fellow, IEEE*

***Abstract*—We focus on a dual-functional multi-input-multi-output (MIMO) radar-communication (RadCom) system, where a single transmitter with multiple antennas communicates with downlink cellular users and detects radar targets simultaneously. Several design criteria are considered for minimizing the downlink multiuser interference. First, we consider both omnidirectional and directional beampattern design problems, where the closed-form globally optimal solutions are obtained. Based on the derived waveforms, we further consider weighted optimizations targeting a flexible tradeoff between radar and communications performance and introduce low-complexity algorithms. Moreover, to address the more practical constant modulus waveform design problem, we propose a branch-and-bound algorithm that obtains a globally optimal solution, and derive its worst-case complexity as function of the maximum iteration number. Finally, we assess the effectiveness of the proposed waveform design approaches via numerical results.**

***Index Terms*—Spectrum sharing, radar-communication, multi-user interference, non-convex optimization, global minimizer.**

I. Introduction

IT HAS been reported that by 2020, the number of connected devices will jump to more than 20 billion, which brings forward an impending need for extra frequency spectrum resources. To address this need, network providers and policy regulators are exploring the feasibility of shared use of spectrum currently occupied exclusively by other applications [1]–[4], such as airborne radars and navigation systems close to the 3.4 GHz band [5] and shipborne and Vessel Traffic Service (VTS) radar at 5.6 GHz [6]; these frequencies may be shared with LTE and Wi-Fi systems in the near future. As an emerging research topic, communications-radar spectrum sharing (CRSS) not only enables the efficient use of the spectrum, but also provides a new way for designing novel systems that can benefit from the co-operation of radar and communications.

As a straightforward way to achieve the spectral coexistence for communication and radar, opportunistic spectrum sharing [7] provides a naive approach, where the communication system transmits when the space and frequency spectra are not occupied by the radar. Nevertheless, it does not allow the two systems to work simultaneously. In view of this, the work of [8] proposes a null-space projection (NSP), an idea that has been widely applied to different spectral coexistence scenarios between MIMO radar and communication systems [9], [10]. In such schemes, a radar beamformer is designed to project the signals onto the null-space of the interference channel between the radar and base station (BS)/user equipment (UE), such that the interference from the radar to the communication link is zero. This, however, results in performance loss for the radar, since the beamforming is no longer optimal for target detection and estimation. Trade-offs between the performance of radar and communications can be achieved by relaxing the zero-forcing precoder to impose controllable interference levels on the communication systems [11], which offers a more realistic coexistence.

More recent contributions have exploited optimization techniques to realize CRSS [12]–[17]. In [12], the radar beamformer and communication covariance matrix are jointly designed to maximize the Signal-to-Interference-plus-Noise-Ratio (SINR) of the radar subject to capacity and power constraints at the communication's side. Similar work has been done for the coexistence between the MIMO-matrix completion (MIMO-MC) radar and point-to-point (P2P) MIMO communications [13], [14], where the radar sub-sampling matrix is further introduced as an optimization variable. To address the more practical coexistence issue between MIMO radar and multi-user MIMO (MU-MIMO) communication, recent work in [17] considers robust beamforming design with imperfect channel state information

Manuscript received November 14, 2017; revised April 27, 2018; accepted June 6, 2018. Date of publication June 15, 2018; date of current version July 10, 2018. The associate editor coordinating the review of this paper and approving it for publication was Prof. Marco Lops. This work was supported in part by the Engineering and Physical Sciences Research Council under Project EP/M014150/1, in part by the China Scholarship Council, and in part by the National Natural Science Foundation of China under Project No. 61771047. This paper was presented in part at the 19th IEEE International Workshop on Signal Processing Advances in Wireless Communications, Kalamata, Greece, Jun. 2018, and in part at the IEEE/CIC International Conference on Communications in China, Beijing, China, Aug. 2018. (*Corresponding author: Fan Liu.*)

F. Liu is with the School of Information and Electronics, Beijing Institute of Technology, Beijing 100081, China, and is also with the Department of Electronic and Electrical Engineering, University College London, London WC1E 7JE, U.K. (e-mail: liufan92@bit.edu.cn).

L. Zhou and W. Luo are with the State Key Laboratory of Advanced Optical Communication Systems and Networks, Peking University, Beijing 100871, China (e-mail: zhoulongfei@pku.edu.cn; luow@pku.edu.cn).

C. Masouros and A. Li are with the Department of Electronic and Electrical Engineering, University College London, London WC1E 7JE, U.K. (e-mail: chris.masouros@ieee.org; ang.li.14@ucl.ac.uk).

A. Petropulu is with the Department of Electrical and Computer Engineering, Rutgers, the State University of New Jersey, Piscataway, NJ 08854 USA (e-mail: athinap@rutgers.edu).

Color versions of one or more of the figures in this paper are available online at http://ieeexplore.ieee.org.

Digital Object Identifier 10.1109/TSP.2018.2847648

(CSI) at the communication's side, where the detection probability of the radar is maximized subject to SINR constraints of the downlink users and the power budget of the BS. As a further development of the technique, a novel beamforming design has been proposed in [18] that exploits the interference as a useful power source, which demonstrates orders-of-magnitude power-savings. While the above coexistence approaches are well-designed, a critical shortfall is that radar and communication devices are required to exchange side-information for achieving a beneficial cooperation, such as the CSI, radar probing waveforms and communication modulation formats. Typically, these exchanges are realized by an all-in-one control center that is connected to both systems via either a wireless link or a backhaul channel [14], which conducts the coordination of the cooperation. In practical scenarios, however, such a control center brings forward considerable extra complexity to the system, and is therefore difficult to implement.

In contrast to the above coexistence schemes, a more favorable approach for CRSS would be to design a dual-functional system that carries out both radar and communications, without exchanges of information. Note that such methods would not be straightforward extension of classic cognitive radio based techniques, as they require the use of specific radar constraints and designs. Recent information theoretical work has shown great potential [19], [20], but it remains to be seen what benefits will bring its implementation in practice. As an enabling solution, dual-functional waveform design can support target detection while carrying information at the same time, which also allows for low-probability-of-intercept (LPI) communications [21]–[23]. Early researches [24]–[26] focused on single-antenna systems, where several integrated waveforms that combine the radar and communication signals have been proposed. Nevertheless, all of these schemes lead to performance loss for either the radar or the communication, e.g., high peak-average-power-ratio (PAPR) and limited dynamic range [25]. As a step further, recent works consider dual-functional waveform design for MIMO systems. In [27], a transmit beampattern for MIMO radar is designed to embed the information bits in sidelobe levels. Related works consider waveform shuffling across the antennas, or Phase Shift Keying (PSK) by different beamformer weighting factors as the communication modulation schemes [28], [29]. It should be noted that in the above approaches, one communication symbol is represented by one or several radar pulses, which leads to a low date rate in the order of the radar pulse repetition frequency (PRF). To support multi-user transmission for the cellular downlink, previous work [30] develops a series of beamforming approaches for dual-functional RadCom systems, which does not affect the original modulation scheme and the data rate of the communication system. Nevertheless, the beamforming approaches only focus on the average power constraints, and do not address the design of the constant modulus signals.

As an important requirement for both radar and communication applications, the utilization of constant modulus waveforms can avoid signal distortion when low-cost non-linear power amplifiers are used [31], which leads to an energy-efficient transmission. Such topics have been widely studied for massive MIMO communication scenarios [32]–[35] as well as the MIMO radar waveform designs [36]–[39], where optimization problems with non-convex constant modulus constraint (CMC) are formulated. Due to the NP-hardness of these problems, only suboptimal solutions can be obtained via either convex relaxation methods or local algorithms, such as Semidefinite Relaxation (SDR) [36], [37] and Riemannian manifold methods [33], [35]. Recent MIMO radar work proposes to approach the constant modulus solution by a successive Quadratic Constrained Quadratic Programming (QCQP) Refinement (SQR) procedure [38]. Nevertheless, this technique still only guarantees the local optimality of the obtained solution. To the best of our knowledge, the efficient global algorithm for constant modulus waveform design is widely unexplored in the existing literature.

In this paper, we propose several optimization-based waveform designs for dual-functional RadCom systems, which can be used for both target detection and downlink communications. Throughout the paper, we aim to minimize the downlink multi-user interference (MUI) under radar-specific constraints. First, we consider an orthogonal waveform design, which is often used for the initial omnidirectional probing by MIMO radar. Based on this waveform, we study the design of a directional radar beampattern that points to the targets of interest. The aforementioned two optimization problems are non-convex, but the optimal solutions can be readily obtained in closed-forms. Still, the obtained performance for the communication system is limited. To allow a trade-off between radar and communication performance, we consider weighted optimizations for designing dual-functional waveforms under non-convex power budget constraints, and obtain the solutions via well-designed low-complexity algorithms. Given that both radar and communication systems require constant modulus signals for power-efficient transmission, we finally consider a more practical optimization by enforcing constant modulus constraints and similarity constraints (SC) on the waveform design. In contrast to the existing approaches in both radar and communication works that obtain the local minimizers of problems with CMC [32]–[39], we propose a branch-and-bound method that can efficiently yield a globally optimal solution for the problem. Our numerical results show that the proposed branch-and-bound algorithm considerably outperforms the conventional SQR method [38]. For clarity, we summarize our contributions as follows:

- We propose dual-functional waveform design approaches for both omnidirectional and directional radar beampatterns, and derive the closed-form solutions.
- We propose weighted optimizations for designing dual-functional waveforms that achieve a flexible trade-off between the radar and communication performance under both total and per-antenna power constraints, and solve the problems with low-complexity algorithms.
- We consider the waveform design with CMC and SC constraints, and develop a branch-and-bound algorithm to obtain the globally optimal solutions, which outperforms the conventional SQR algorithm.
- We analytically derive the computational complexity for the proposed algorithms.

The remainder of this paper is organized as follows, Section II introduces the system model, Section III proposes the closed-form waveform optimizations for radar beampattern

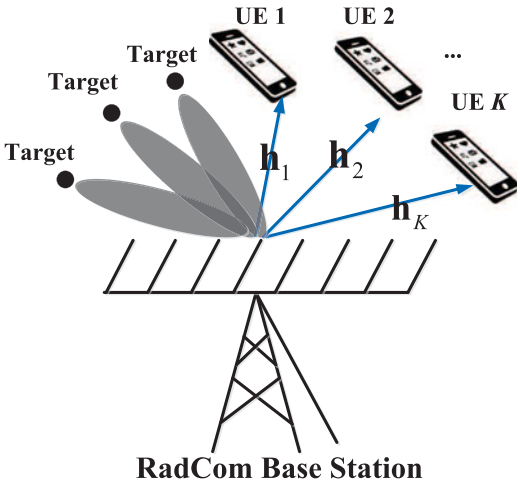

Fig. 1. Dual-functional Radar-Communication System.

design, Section IV considers the trade-off designs between radar and communications, Section V solves the problem with CMC and SC constraints, Section VI provides numerical results, and finally Section VII concludes the paper.

Notations: Unless otherwise specified, matrices are denoted by bold uppercase letters (i.e., $\mathbf{H}$), vectors are represented by bold lowercase letters (i.e., $\mathbf{x}$), and scalars are denoted by normal font (i.e., ρ). Subscripts indicate the location of the entry in the matrices or vectors (i.e., $s_{i,j}$ and l_n are the (i,j)-th and the n-th element in $\mathbf{S}$ and $\mathbf{l}$, respectively). $\mathrm{tr}\,(\cdot)$ and $\mathrm{vec}\,(\cdot)$ denote the trace and the vectorization operations. $(\cdot)^T$, $(\cdot)^H$, $(\cdot)^*$ and $(\cdot)^\dagger$ stand for transpose, Hermitian transpose, complex conjugate and Moore-Penrose pseudo-inverse of the matrices, respectively. $\mathrm{diag}\,(\cdot)$ represents the vector formed by the diagonal elements of the matrices, and $\mathrm{ddiag}\,(\cdot)$ sets all off-diagonal elements as zero. $\mathrm{Re}\,(\cdot)$ and $\mathrm{Im}\,(\cdot)$ denote the real and imaginary part of the argument. $\|\cdot\|$, $\|\cdot\|_\infty$ and $\|\cdot\|_F$ denote the l_2 norm, l_∞ and the Frobenius norm respectively.

II. System Model

We consider a dual-functional MIMO RadCom system, which simultaneously transmits radar probing waveforms to the targets and communication symbols to the downlink users. As shown in Fig. 1, the joint system is equipped with a uniform linear array (ULA) with N antennas, serving K single-antenna users while detecting radar targets at the same time.

A. Communication Model

The received symbol matrix at the downlink users can be given as

$$\mathbf{Y} = \mathbf{H}\mathbf{X} + \mathbf{W}, \tag{1}$$

where $\mathbf{H} = [\mathbf{h}_1, \mathbf{h}_2, ..., \mathbf{h}_K]^T \in \mathbb{C}^{K\times N}$ is the channel matrix, $\mathbf{X} = [\mathbf{x}_1, \mathbf{x}_2, \ldots, \mathbf{x}_L] \in \mathbb{C}^{N\times L}$ is the transmitted signal matrix, with L being the length of the communication frame, $\mathbf{W} = [\mathbf{w}_1, \mathbf{w}_2, \ldots, \mathbf{w}_L] \in \mathbb{C}^{K\times L}$ is the noise matrix, with $\mathbf{w}_j \sim \mathcal{CN}\left(0, N_0\mathbf{I}_N\right), \forall j$.

Following [30], we rely on the following assumptions: 1) The transmitted signal matrix $\mathbf{X}$ is used as dual-functional waveform for both radar and communication operations. In this case, each communication symbol is also a snapshot of a radar pulse; 2) The downlink channel $\mathbf{H}$ is flat Rayleigh fading, and remains unchanged during one communication frame/radar pulse; 3) The channel $\mathbf{H}$ is assumed to be perfectly estimated by pilot symbols.

Given the desired constellation symbol matrix $\mathbf{S} \in \mathbb{C}^{K\times L}$ for the downlink users, the received signals can be rewritten as

$$\mathbf{Y} = \mathbf{S} + \underbrace{(\mathbf{H}\mathbf{X} - \mathbf{S})}_{\text{MUI}} + \mathbf{W}, \tag{2}$$

For each user, the entry of $\mathbf{S}$ is assumed to be drawn from the same constellation. The second term in (2) represents the MUI signals. The total MUI energy can be measured as

$$P_{\text{MUI}} = \|\mathbf{H}\mathbf{X} - \mathbf{S}\|_F^2 . \tag{3}$$

It has been proven in [32] that the MUI energy in (3) directly affects the achievable sum-rate of the downlink users. For the i-th user, the SINR per frame is given as [32]

$$\gamma_i = \frac{\mathbb{E}\left(|s_{i,j}|^2\right)}{\underbrace{\mathbb{E}\left(\left|\mathbf{h}_i^T\mathbf{x}_j - s_{i,j}\right|^2\right)}_{\text{MUI energy}} + N_0}, \tag{4}$$

where $s_{i,j}$ is the (i,j)-th entry of $\mathbf{S}$, $\mathbb{E}$ denotes the ensemble average with respect to the time index. It follows that the achievable sum-rate of the users can be given as

$$R = \sum_{i=1}^{K} \log_2\left(1+\gamma_i\right). \tag{5}$$

For a given constellation with fixed energy, the power of the useful signal $\mathbb{E}\left(|s_{i,j}|^2\right)$ is also fixed. Hence, the sum-rate can be maximized by minimizing the MUI energy.

B. Radar Model

It is widely known that by employing uncorrelated waveforms, MIMO radar achieves higher Degrees of Freedom (DoFs) than the traditional phased-array radar [40], [41]. The existing literature indicates that the design of such a beampattern is equivalent to designing the covariance matrix of the probing signals, where convex optimization can be employed. We refer readers to [41]–[43] for more details on this topic. Here we focus on designing the dual-functional waveform matrix $\mathbf{X}$, which has the following spatial covariance matrix

$$\mathbf{R}_X = \frac{1}{L}\mathbf{X}\mathbf{X}^H. \tag{6}$$

To ensure that $\mathbf{R}_X$ is positive-definite, we assume $L \geq N$ without loss of generality. Further, the transmit beampattern for the RadCom system can be given as

$$P_d\left(\theta\right) = \mathbf{a}^H\left(\theta\right)\mathbf{R}_X\,\mathbf{a}\left(\theta\right), \tag{7}$$

where θ denotes the detection angle, $\mathbf{a}\left(\theta\right) = \left[1, e^{j2\pi\Delta\sin(\theta)}, \ldots, e^{j2\pi(N-1)\Delta\sin(\theta)}\right]^T \in \mathbb{C}^{N\times 1}$ is the

steering vector of the transmit antenna array with Δ being the spacing between adjacent antennas normalized by the wavelength.

In the following, we formulate optimization problems that minimize P_{MUI} under MIMO radar-specific constraints.

III. Closed-form Waveform Design for Given Radar Beampatterns

In this section, we first consider the omnidirectional beampattern design, which is usually used in MIMO radar for initial probing. After that, we consider a directional beampattern design that points to the directions of interest.

A. Omnidirectional Beampattern Design

For an omnidirectional beampattern, the transmitted waveform matrix $\mathbf{X}$ has to be orthogonal, i.e., the corresponding covariance matrix must be the identity matrix. To minimize the MUI energy, the optimization problem is formulated as

$$\begin{aligned} &\min_{\mathbf{X}} \|\mathbf{H}\mathbf{X}-\mathbf{S}\|_F^2 \\ &s.t.\ \ \frac{1}{L}\mathbf{X}\mathbf{X}^H = \frac{P_T}{N}\mathbf{I}_N, \end{aligned} \tag{8}$$

where P_T is the total transmit power, $\mathbf{I}_N$ denotes the $N \times N$ identity matrix. Problem (8) is obviously non-convex due to the equality constraint, which indicates that $\mathbf{X}$ is a point on the Stiefel manifold. Fortunately, it has been proven that (8) can be classified as the so-called Orthogonal Procrustes problem (OPP), which has a simple closed-form global solution based on the Singular Value Decomposition (SVD), and is given as [44]

$$\mathbf{X} = \sqrt{\frac{LP_T}{N}}\mathbf{U}\mathbf{I}_{N\times L}\mathbf{V}^H, \tag{9}$$

where $\mathbf{U}\mathbf{\Sigma}\mathbf{V}^H = \mathbf{H}^H\mathbf{S}$ is the SVD of $\mathbf{H}^H\mathbf{S}$ with $\mathbf{U} \in \mathbb{C}^{N\times N}$ and $\mathbf{V} \in \mathbb{C}^{L\times L}$ being the unitary matrices, $\mathbf{I}_{N\times L}$ is an $N \times L$ rectangular matrix composed by an $N \times N$ identity matrix and an $N \times (L-N)$ zero matrix.

B. Directional Beampattern Design

Given a covariance matrix $\mathbf{R}_d$ that corresponds to a well-designed MIMO radar beampattern, the MUI minimization problem is given as

$$\begin{aligned} &\min_{\mathbf{X}} \|\mathbf{H}\mathbf{X}-\mathbf{S}\|_F^2 \\ &s.t.\ \ \frac{1}{L}\mathbf{X}\mathbf{X}^H = \mathbf{R}_d, \end{aligned} \tag{10}$$

where $\mathbf{R}_d$ is the desired Hermitian positive semidefinite covariance matrix. We consider its Cholesky decomposition, which is

$$\mathbf{R}_d = \mathbf{F}\mathbf{F}^H, \tag{11}$$

where $\mathbf{F} \in \mathbb{C}^{N\times N}$ is a lower triangular matrix. Without loss of generality, we assume $\mathbf{R}_d$ is positive-definite to ensure that $\mathbf{F}$ is invertible. Hence, the constraint in (10) can be equivalently written as

$$\frac{1}{L}\mathbf{F}^{-1}\mathbf{X}\mathbf{X}^H\mathbf{F}^{-H} = \mathbf{I}_N. \tag{12}$$

Denoting $\tilde{\mathbf{X}} = \sqrt{\frac{1}{L}}\mathbf{F}^{-1}\mathbf{X}$, problem (10) can be reformulated as

$$\begin{aligned} &\min_{\tilde{\mathbf{X}}} \left\|\sqrt{L}\mathbf{H}\mathbf{F}\tilde{\mathbf{X}}-\mathbf{S}\right\|_F^2 \\ &s.t.\ \ \tilde{\mathbf{X}}\tilde{\mathbf{X}}^H = \mathbf{I}_N, \end{aligned} \tag{13}$$

which is again an OPP problem, and its globally optimal solution is given by

$$\tilde{\mathbf{X}} = \tilde{\mathbf{U}}\mathbf{I}_{N\times L}\tilde{\mathbf{V}}^H, \tag{14}$$

where $\tilde{\mathbf{U}}\tilde{\mathbf{\Sigma}}\tilde{\mathbf{V}}^H = \mathbf{F}^H\mathbf{H}^H\mathbf{S}$ is the SVD of $\mathbf{F}^H\mathbf{H}^H\mathbf{S}$. It follows that the solution of the original problem (10) is given as

$$\mathbf{X} = \sqrt{L}\mathbf{F}\tilde{\mathbf{U}}\mathbf{I}_{N\times L}\tilde{\mathbf{V}}^H. \tag{15}$$

C. Complexity Analysis

The omnidirectional beampattern design includes two matrix multiplications and one SVD, which needs a total of $\mathcal{O}\left(NKL + NL^2\right)$ complex floating-point-operations (flops), where one complex flop is defined as one complex addition or multiplication. The directional beampattern design, which needs one Cholesky decomposition, four matrix multiplications and one SVD, has the total complexity of $\mathcal{O}\left(NL^2 + N^2L + NKL + N^3 + N^2K\right)$. For the conventional communication-only zero-forcing (ZF) precoding, which involves one pseudo-inverse for $\mathbf{H}$, and one matrix multiplication between the precoder and the transmitted symbol matrix, the complexity is $\mathcal{O}\left(NKL + N^2K\right)$. It is worth noting that the computational costs of the proposed closed-form approaches share the same order of magnitude with that of the zero-forcing precoder.

IV. Trade-off Between Radar and Communication Performance

It should be highlighted that both problem (8) and (10) enforce a strict equality constraint, in which case the radar beampattern can be strictly achieved while the downlink communication may suffer from serious performance loss. This is particularly pronounced in the cases that the covariance matrices of the communication channel are ill-conditioned, where the resulting MUI minimum is still high. We therefore consider a trade-off design by allowing a tolerable mismatch between the designed and the desired radar beampatterns. While the radar typically requires equivalent transmit power at each antenna, we start from the case that only the total power is constrained for simplicity. To ensure the coherence with the previous problems (8) and (10), we then consider the waveform design with the per-antenna power constraint.

A. Trade-off Design with Total Power Constraint

Let us first denote the optimal solution obtained from (8) and (10) as $\mathbf{X}_0$[1]. Given $\mathbf{X}_0$, the trade-off problem with total power constraint can be then formulated as

$$\begin{aligned} &\min_{\mathbf{X}} \rho \left\|\mathbf{H}\mathbf{X}-\mathbf{S}\right\|_F^2 + (1-\rho)\left\|\mathbf{X}-\mathbf{X}_0\right\|_F^2 \\ &s.t.\ \ \frac{1}{L}\left\|\mathbf{X}\right\|_F^2 = P_T, \end{aligned} \tag{16}$$

where $0 \le \rho \le 1$ is a weighting factor that determines the weights for radar and communication performance in the dual-functional system. We enforce an equality constraint for the total power budget, as the radar is often required to transmit at its maximum available power in practice. It is worth noting that the trade-off design is in fact a Pareto optimization. By solving the weighted problem in (16), the obtained solution reaches the Pareto optimal point [45].

Note that the two Frobenius norms in the objective function can be combined in the form

$$\begin{aligned} &\rho \left\|\mathbf{H}\mathbf{X}-\mathbf{S}\right\|_F^2 + (1-\rho)\left\|\mathbf{X}-\mathbf{X}_0\right\|_F^2 \\ &= \left\| \left[\sqrt{\rho}\mathbf{H}^T, \sqrt{1-\rho}\mathbf{I}_N\right]^T \mathbf{X} - \left[\sqrt{\rho}\mathbf{S}^T, \sqrt{1-\rho}\mathbf{X}_0^T\right]^T \right\|_F^2. \end{aligned} \tag{17}$$

Let us denote $\mathbf{A} = \left[\sqrt{\rho}\mathbf{H}^T, \sqrt{1-\rho}\mathbf{I}_N\right]^T \in \mathbb{C}^{(K+N)\times N}$, $\mathbf{B} = \left[\sqrt{\rho}\mathbf{S}^T, \sqrt{1-\rho}\mathbf{X}_0^T\right]^T \in \mathbb{C}^{(K+N)\times L}$, problem (16) can be written compactly as

$$\begin{aligned} &\min_{\mathbf{X}} \left\|\mathbf{A}\mathbf{X}-\mathbf{B}\right\|_F^2 \\ &s.t.\ \ \left\|\mathbf{X}\right\|_F^2 = LP_T, \end{aligned} \tag{18}$$

which is a non-convex QCQP, and can be readily transformed into a Semidefinite Programming (SDP) using the SDR technique. Since it has only one quadratic constraint, according to [46], [47], the SDR is tight, i.e., the solution of the SDR is rank-1, which yields the globally optimal solution of (18).

B. Low-complexity Algorithm for Solving (16)

Due to the large number of variables in the problem (18), the above SDR solver is not computationally efficient in general. Hence, in this subsection, we propose a low-complexity algorithm that achieves the global optimum in the following. Let us further expand the objective function of (18) as

$$\begin{aligned} \left\|\mathbf{A}\mathbf{X}-\mathbf{B}\right\|_F^2 &= \mathrm{tr}\left(\left(\mathbf{A}\mathbf{X}-\mathbf{B}\right)^H\left(\mathbf{A}\mathbf{X}-\mathbf{B}\right)\right) \\ &= \mathrm{tr}\left(\mathbf{X}^H\mathbf{A}^H\mathbf{A}\mathbf{X}\right) - \mathrm{tr}\left(\mathbf{X}^H\mathbf{A}^H\mathbf{B}\right) \\ &\quad - \mathrm{tr}\left(\mathbf{B}^H\mathbf{A}\mathbf{X}\right) + \mathrm{tr}\left(\mathbf{B}^H\mathbf{B}\right). \end{aligned} \tag{19}$$

[1]Please note that $\mathbf{X}_0$ is not necessarily to be the solution of (8) and (10). In practical scenarios, $\mathbf{X}_0$ can be any reference radar waveforms with desired properties according to the requirements of the system operators. Nevertheless, here we use these solutions for coherence with the previous designs.

Defining $\mathbf{Q} = \mathbf{A}^H\mathbf{A}, \mathbf{G} = \mathbf{A}^H\mathbf{B}$, problem (18) can be rewritten as

$$\begin{aligned} &\min_{\mathbf{X}} \mathrm{tr}\left(\mathbf{X}^H\mathbf{Q}\mathbf{X}\right) - 2\,\mathrm{Re}\left(\mathrm{tr}\left(\mathbf{X}^H\mathbf{G}\right)\right) \\ &s.t.\ \ \left\|\mathbf{X}\right\|_F^2 = LP_T. \end{aligned} \tag{20}$$

Since $\mathbf{Q}$ is a Hermitian matrix, problem (20) can be viewed as the matrix version of the trust-region subproblem (TRS), for which the strong duality holds [48], i.e., the duality gap is zero. Let us formulate the Lagrangian multiplier as

$$\begin{aligned} \mathcal{L}\left(\mathbf{X},\lambda\right) &= \mathrm{tr}\left(\mathbf{X}^H\mathbf{Q}\mathbf{X}\right) - 2\,\mathrm{Re}\left(\mathrm{tr}\left(\mathbf{X}^H\mathbf{G}\right)\right) \\ &\quad + \lambda\left(\left\|\mathbf{X}\right\|_F^2 - LP_T\right), \end{aligned} \tag{21}$$

where λ is the dual variable associated with the equality constraint. Let $\mathbf{X}_{opt}$ and λ_{opt} be the primal and dual optimal points with zero duality gap, the optimality conditions for the above TRS can be given as [49]

$$\nabla\mathcal{L}\left(\mathbf{X}_{opt},\lambda_{opt}\right) = 2\left(\mathbf{Q}+\lambda_{opt}\mathbf{I}_N\right)\mathbf{X}_{opt} - 2\mathbf{G} = 0, \tag{22a}$$

$$\left\|\mathbf{X}_{opt}\right\|_F^2 = LP_T, \tag{22b}$$

$$\mathbf{Q}+\lambda_{opt}\mathbf{I}_N \succeq 0, \tag{22c}$$

where (22b) and (22c) guarantee the primal and the dual feasibility respectively. It follows from (22a) that

$$\mathbf{X}_{opt} = \left(\mathbf{Q}+\lambda_{opt}\mathbf{I}_N\right)^{\dagger}\mathbf{G}, \tag{23}$$

where $(\cdot)^{\dagger}$ denotes the Moore-Penrose pseudo-inverse of the matrix. Based on (22b) and (22c) we have

$$\begin{aligned} &\left\|\left(\mathbf{Q}+\lambda_{opt}\mathbf{I}_N\right)^{\dagger}\mathbf{G}\right\|_F^2 \\ &\quad = \left\|\mathbf{V}(\mathbf{\Lambda}+\lambda_{opt}\mathbf{I}_N)^{-1}\mathbf{V}^H\mathbf{G}\right\|_F^2 = LP_T, \\ &\quad \lambda_{opt} \ge -\lambda_{\min}. \end{aligned} \tag{24}$$

where $\mathbf{Q} = \mathbf{V}\mathbf{\Lambda}\mathbf{V}^H$ is the eigenvalue decomposition of $\mathbf{Q}$ with $\mathbf{V}$ and $\mathbf{\Lambda}$ being the orthogonal and diagonal matrices that contain the eigenvectors and eigenvalues respectively, and $\lambda_{\min}$ is the minimum eigenvalue of $\mathbf{Q}$. One can further show that there exists a unique solution for the equations (24). Let us define

$$\begin{aligned} P\left(\lambda\right) &= \left\|\mathbf{V}(\mathbf{\Lambda}+\lambda\mathbf{I}_N)^{-1}\mathbf{V}^H\mathbf{G}\right\|_F^2 \\ &= \sum_{i=1}^{N}\sum_{j=1}^{L}\frac{\left(\left[\mathbf{V}^H\mathbf{G}\right]_{i,j}\right)^2}{\left(\lambda+\lambda_i\right)^2}, \end{aligned} \tag{25}$$

where λ_i is the *i*-th eigenvalue of $\mathbf{Q}$. It can be seen that $P\left(\lambda\right)$ is strictly decreasing and convex on the interval $\lambda \ge -\lambda_{\min}$, which suggests that λ_{opt} can be obtained by simple line search methods, e.g., Golden-section search [50]. Thanks to the eigenvalue decomposition, in each iteration we only need to calculate the inversion of a diagonal matrix. Once the optimal λ is obtained, the optimal solution to (16) can be computed by (23). For clarity, we summarize the above approach in Algorithm 1.

Algorithm 1: Low-complexity Algorithm for Solving (16).

Input: $\mathbf{H}, \mathbf{S}, \mathbf{X}_0$, weighting factor $0 \leq \rho \leq 1$, P_T

Output: Global minimizer $\mathbf{X}_{opt}$

1. Compute $\mathbf{A}$, $\mathbf{B}$, $\mathbf{Q}$ and $\mathbf{G}$.
2. Compute the eigenvalue decomposition of $\mathbf{Q}$, set the searching interval as $[-\lambda_{\min}, b]$, where $b \geq 0$ is a searching upper-bound.
3. Find the optimal solution λ_{opt} to (24) using Golden-section search.
4. $\mathbf{X}_{opt} = (\mathbf{Q} + \lambda_{opt}\mathbf{I}_N)^{\dagger}\mathbf{G}$.

C. Trade-off Design with Per-antenna Power Constraint

Similar to (16), the trade-off problem with per-antenna power constraint can be given as

$$\begin{aligned} &\min_{\mathbf{X}} \rho \left\|\mathbf{HX}-\mathbf{S}\right\|_F^2 + (1-\rho)\left\|\mathbf{X}-\mathbf{X}_0\right\|_F^2 \\ &s.t.\ \ \frac{1}{L}\operatorname{diag}\left(\mathbf{X}\mathbf{X}^H\right) = \frac{P_T}{N}\mathbf{1}, \end{aligned} \tag{26}$$

where $\operatorname{diag}(\cdot)$ denotes the vector formed by the diagonal elements of the matrices, and $\mathbf{1} = [1, 1, \ldots, 1]^T \in \mathbb{R}^{N\times 1}$ stands for the all-one vector. By the same definitions as in (18), the problem (26) can be recast as

$$\begin{aligned} &\min_{\mathbf{X}} \ \left\|\mathbf{AX}-\mathbf{B}\right\|_F^2 \\ &s.t.\ \ \operatorname{diag}\left(\mathbf{X}\mathbf{X}^H\right) = \frac{LP_T}{N}\mathbf{1}. \end{aligned} \tag{27}$$

The diagonal constraint can be separated as N quadratic equality constraints, which again result in non-convex feasible region. By using the SDR approach, one can relax (27) as a convex SDP problem that can be readily solved by numerical tools. Nevertheless, due to the multiple constraints involved, SDR is no longer tight, in which case Gaussian randomization must be employed to obtain an approximated rank-1 solution.

D. Low-complexity Manifold Algorithm for Solving (26)

Noting that the SDR approach solves the problem at the price of high computational costs, we propose in this subsection an Riemannian Conjugate Gradient (RCG) algorithm [51], [52], which finds a near-optimal solution within much lower complexity. First of all, note that the feasible region in (27), denoted as $\mathcal{M}$, forms the so-called *complex oblique manifold* [53]. The problem (27) can be therefore reformulated as the following least-squares (LS) problem on the manifold

$$\min_{\mathbf{X}\in\mathcal{M}} \left\|\mathbf{AX}-\mathbf{B}\right\|_F^2. \tag{28}$$

Given a point $\mathbf{X} \in \mathcal{M}$, a *tangent vector* at $\mathbf{X}$ is defined as the vector that is tangential to any smooth curves on $\mathcal{M}$ through $\mathbf{X}$. All such vectors formulate the *tangent space* $T_{\mathbf{X}}\mathcal{M}$, which is a Euclidean space [54]. According to [53], the tangent space for the oblique manifold can be given in the form

$$T_{\mathbf{X}}\mathcal{M} = \left\{\mathbf{Z} \in \mathbb{C}^{N\times L} \left| \operatorname{Re}\left(\left(\mathbf{X}^H\mathbf{Z}\right)_{ii}\right) = 0, \forall i \right.\right\}, \tag{29}$$

where $(\cdot)_{ii}$ denotes the i-th diagonal element of the matrices.

Denoting the objective function as $F(\mathbf{X}) = \left\|\mathbf{AX}-\mathbf{B}\right\|_F^2$, it follows that

$$\nabla F(\mathbf{X}) = 2\mathbf{A}^H\left(\mathbf{AX}-\mathbf{B}\right), \tag{30}$$

which we call *Euclidean gradient* in the proposed RCG framework [51]. Unlike the conventional gradient based algorithm, the RCG method adopts the *Riemannian gradient* for computing the descent direction, which is defined as the orthogonal projection of (30) onto the associated tangent space $T_{\mathbf{X}}\mathcal{M}$, and is given as [53]

$$\begin{aligned} &\operatorname{grad} F(\mathbf{X}) = \mathcal{P}_{\mathbf{X}}\nabla F(\mathbf{X}) \\ &= \nabla F(\mathbf{X}) - \mathbf{X}^H \operatorname{ddiag}\left(\operatorname{Re}\left(\nabla F(\mathbf{X})^H\mathbf{X}\right)\right), \end{aligned} \tag{31}$$

where $\operatorname{ddiag}(\cdot)$ sets all off-diagonal elements of the matrices as zero. We then define the Retraction mapping, which maps the point on $T_{\mathbf{X}}\mathcal{M}$ to $\mathcal{M}$. This is given by [53]

$$\mathcal{R}_{\mathbf{X}}(\mathbf{Z}) = \sqrt{\frac{LP_T}{N}}\operatorname{ddiag}\left(\left(\mathbf{X}+\mathbf{Z}\right)\left(\mathbf{X}+\mathbf{Z}\right)^H\right)^{-1/2}\left(\mathbf{X}+\mathbf{Z}\right), \tag{32}$$

where $\mathbf{Z} \in T_{\mathbf{X}}\mathcal{M}$. Finally, we use the trace operator as the inner product on the tangent space, which is

$$\langle \mathbf{X}, \mathbf{Z} \rangle = \operatorname{Re}\left(\operatorname{tr}\left(\mathbf{X}^H\mathbf{Z}\right)\right). \tag{33}$$

Following the similar procedure in [30], [55], [56], the proposed RCG approach is summarized in Algorithm 2. In brief, the RCG method is the modified version of the conventional Conjugate Gradient (CG) algorithm defined on the manifold feasible region. Given the limited space, we refer the reader to [30], [55], [56] for more background details on this topic.

E. Complexity Analysis

We end this section by analyzing the complexity of the proposed algorithms. For Algorithm 1, the Golden-section search method is known to have linear convergence rate, which finds an ε_0-solution within $\mathcal{O}(\log(1/\varepsilon_0))$ iterations. In each iteration we calculate the value of a 1-dimensional function, which suggests that the complexity of the Golden-section search can be omitted in general. Hence the complexity for Algorithm 1 is dominated by the matrix multiplications, the pseudo-inverse and the eigenvalue decomposition. Both of the latter two operations involve the computational costs of $\mathcal{O}\left(N^3\right)$ complex flops, and the matrix multiplications involve the complexity of $\mathcal{O}\left(N^2L + NKL + N^3 + N^2K\right)$. Therefore, the total complexity for Algorithm 1 is $\mathcal{O}\left(N^2L + NKL + N^3 + N^2K\right)$, which again shares the same order of magnitude with the communication-only ZF precoding.

To the best of our knowledge, the strict convergence analysis for the RCG algorithm still remains open problem in the field of manifold optimization [51], [52]. Hence, it is rather intractable to analyze the convergence rate of Algorithm 2. We hereby provide the computational costs within a single iteration. It can be trivially seen that the dominated computational cost comes from the computation of the gradient (30), which is $\mathcal{O}\left(N^2L + NKL\right)$. In contrast, the computation

Algorithm 2: RCG Algorithm for Solving (26).

Input: $\mathbf{H}, \mathbf{S}, \mathbf{X}_0$, weighting factor $0 \leq \rho \leq 1$, P_T, $\delta > 0$, $k_{\max} > 2$

Output: $\mathbf{X}^{(k)}$

1. Compute $\mathbf{A}, \mathbf{B}$. Initialize randomly $\mathbf{X}^{(0)} = \mathbf{X}^{(1)} \in \mathcal{M}$, set $\mathbf{\Pi}_0 = -\operatorname{grad} F\left(\mathbf{X}^{(0)}\right)$, $k = 1$.

while $k \leq k_{\max}$ and $\left\|\operatorname{grad} F\left(\mathbf{X}^{(k)}\right)\right\|_F \geq \delta$ **do**

2. Compute the difference between the current and the previous gradients by

$$\mathbf{J}_k = \operatorname{grad} F\left(\mathbf{X}^{(k)}\right) - \mathcal{P}_{\mathbf{X}^{(k)}}\left(\operatorname{grad} F\left(\mathbf{X}^{(k-1)}\right)\right).$$

3. Compute the combination coefficient τ_k using the Polak-Ribiére formula as

$$\tau_k = \frac{\left\langle \operatorname{grad} F\left(\mathbf{X}^{(k)}\right), \mathbf{J}_k \right\rangle}{\left\langle \operatorname{grad} F\left(\mathbf{X}^{(k-1)}\right), \operatorname{grad} F\left(\mathbf{X}^{(k-1)}\right) \right\rangle}.$$

4. Compute the descent direction $\mathbf{\Pi}_k$ by

$$\mathbf{\Pi}_k = -\operatorname{grad} F\left(\mathbf{X}^{(k)}\right) + \tau_k \mathcal{P}_{\mathbf{X}^{(k)}}\left(\operatorname{grad} F\left(\mathbf{X}^{(k-1)}\right)\right).$$

5. Compute stepsize μ_k by the Armijo line search method, and set $\mathbf{X}^{(k+1)}$ by

$$\mathbf{X}^{(k+1)} = \mathcal{R}_{\mathbf{X}^{(k)}}\left(\mu_k \mathbf{\Pi}_k\right).$$

6. $k = k + 1$.

end while

TABLE I
COMPUTATIONAL COMPLEXITY FOR THE PROPOSED APPROACHES

Method	Complex Flops
Omnidirectional Design	$\mathcal{O}\left(NKL + NL^2\right)$
Directional Design	$\mathcal{O}\left(NL^2 + N^2L + NKL + N^3 + N^2K\right)$
Algorithm 1	$\mathcal{O}\left(N^2L + NKL + N^3 + N^2K\right)$
Algorithm 2	$\mathcal{O}\left(N_{iter}N^2L + N_{iter}NKL\right)$
Zero-forcing (benchmark)	$\mathcal{O}\left(NKL + N^2K\right)$

costs of the projection (31), the retraction (32) and the inner product (33) correspond to the lower-order terms in the complexity expression. Hence, the complexity for Algorithm 2 is $\mathcal{O}\left(N_{iter}N^2L + N_{iter}NKL\right)$, where N_{iter} is the total iteration number needed [2].

For the sake of clarity, we summarize the computational costs of the proposed four waveform design approaches in Table I.

V. CONSTANT MODULUS WAVEFORM DESIGN

In the previous sections, the dual-functional RadCom waveform is designed under the average power constraints, which is not guaranteed to generate constant modulus signals. In this section, we consider the RadCom waveform design that minimizes the communication MUI energy given the CMC.

A. Problem Formulation

Following the same notations as in the previous section, our optimization problem can be formulated as

$$\min_{\mathbf{X}} \|\mathbf{HX} - \mathbf{S}\|_F^2 \tag{34a}$$

$$s.t \ \ \|\operatorname{vec}(\mathbf{X} - \mathbf{X}_0)\|_\infty \leq \eta, \tag{34b}$$

$$|x_{i,j}| = \sqrt{\frac{P_T}{N}}, \forall i, j, \tag{34c}$$

where $\mathbf{X}_0 \in \mathbb{C}^{N \times L}$ is a known benchmark radar signal matrix that has constant-modulus entries, e.g., chirp signals, $\operatorname{vec}(\cdot)$ denotes the vectorization of a matrix, and $x_{i,j}$ is the (i,j)-th entry of $\mathbf{X}$. The constraint (34b) is called similarity constraint (SC) in the radar literature [37], which controls the difference between the designed waveform and the benchmark with η being the tolerable difference.

It is easy to see that the objective function of (34) is separable, since

$$\|\mathbf{HX} - \mathbf{S}\|_F^2 = \sum_{i=1}^{L} \|\mathbf{H}\mathbf{x}_i - \mathbf{s}_i\|^2. \tag{35}$$

Hence, it can be further simplified using the normalized vector variable, which is

$$\begin{aligned} \min_{\mathbf{x}} \ & \left\| \sqrt{\frac{P_T}{N}}\mathbf{H}\mathbf{x} - \mathbf{s} \right\|^2 \\ s.t \ \ & \|\mathbf{x} - \mathbf{x}_0\|_\infty \leq \varepsilon, \\ & |x(n)| = 1, \forall n, \end{aligned} \tag{36}$$

where $\varepsilon = \eta\sqrt{\frac{N}{P_T}}$, $\mathbf{x} \in \mathbb{C}^{N \times 1}$, $\mathbf{x}_0 \in \mathbb{C}^{N \times 1}$ are the columns of $\mathbf{X}$ and $\mathbf{X}_0$ normalized by $\sqrt{\frac{P_T}{N}}$, $\mathbf{s} \in \mathbb{C}^{K \times 1}$ is the column of $\mathbf{S}$, and $x(n)$ denotes the n-th entry of $\mathbf{x}$. Since problem (34) can be solved by solving the problem (36) for each column of $\mathbf{X}$ concurrently, we will focus on (36) in the following discussion. For notational convenience, we omit the column index.

Note that $0 \leq \varepsilon \leq 2$ since both $\mathbf{x}$ and $\mathbf{x}_0$ have unit modulus. According to [37], the similarity constraint can be rewritten as[3]

$$\arg\, x(n) \in [l_n, u_n], \forall n, \tag{37}$$

where

$$\begin{aligned} l_n &= \arg\, x_0(n) - \arccos\left(1 - \varepsilon^2/2\right), \\ u_n &= \arg\, x_0(n) + \arccos\left(1 - \varepsilon^2/2\right), \end{aligned} \tag{38}$$

which leads to the following equivalent formulation of the problem

$$\begin{aligned} \min_{\mathbf{x}} \ & f(\mathbf{x}) = \left\| \tilde{\mathbf{H}}\mathbf{x} - \mathbf{s} \right\|^2 \\ s.t \ \ & \arg\, x(n) \in [l_n, u_n], \forall n, \\ & |x(n)| = 1, \forall n, \end{aligned} \tag{39}$$

[2] We observe in our simulations that Algorithm 2 always converges in tens of iterations for a modest accuracy.

[3] At this point we note the use of the infinity norm, which allows the element-wise reformulation of the norm constraint.

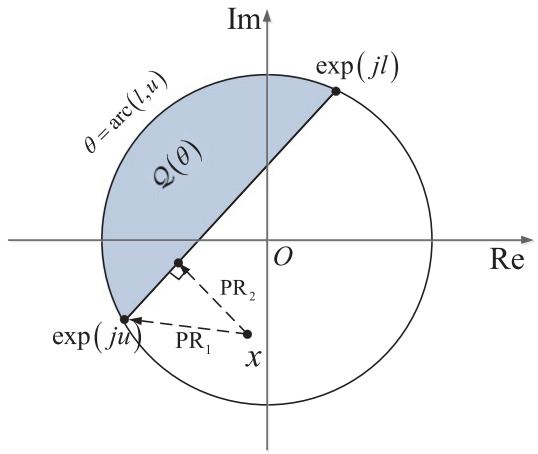

Fig. 2. Feasible region and convex hull of problem (36).

where $\tilde{\mathbf{H}} = \sqrt{\frac{P_T}{N}}\mathbf{H}$. For each $x(n)$, the feasible region is an arc on the unit circle as shown in Fig. 2, which makes the problem non-convex, and NP-hard in general. In the following, we consider a global optimization algorithm for solving (36), which is based on the general framework of the branch-and-bound (BnB) methodology [57].

B. The Branch-and-bound Framework

A typical BnB algorithm requires to partition the feasible region into several subregions, where we formulate corresponding subproblems. For each subproblem, we obtain a sequence of asymptotic lower-bounds and upper-bounds by well-designed bounding functions. In each iteration, we update the bounds and the set of the subproblems following the BnB rules until convergence, i.e., the difference between the upper-bound and lower-bound goes to zero.

It is well-known that the worst-case complexity for the BnB algorithm is of the exponential order with respect to N, i.e., to search all the branches of the subproblems exhaustively [57]. Nevertheless, by carefully choosing the tightest bounds, it is possible to efficiently identify and prune the unqualified branches, which accelerates the algorithm significantly.

Let us denote the feasible region, i.e., the arc shown in Fig. 2, as $\theta_n = \arc(l_n, u_n)$. Problem (39) can be compactly written as

$$\mathcal{P}(\Theta_0): \min_{\mathbf{x}} f(\mathbf{x}) \quad s.t.\ \mathbf{x} \in \Theta_0, \tag{40}$$

where $\Theta_0 = \theta_1 \times \theta_2 \times ... \times \theta_N$, and $f(\mathbf{x})$ is defined in (39). By the above notations, a subproblem can be denoted as $\mathcal{P}(\Theta)$, where $\Theta \subseteq \Theta_0$ is the corresponding subregion. We then find a lower-bound of $\mathcal{P}(\Theta)$ by a lower-bounding function

$$f_L(\Theta) = f(\mathbf{x}_l), \tag{41}$$

where $\mathbf{x}_l$ is a relaxed solution that achieves the bound. In order to compute the upper-bound, we find a feasible solution $\mathbf{x}_u$ for $\mathcal{P}(\Theta)$. The upper-bounding function is thus given by

$$f_U(\Theta) = f(\mathbf{x}_u). \tag{42}$$

The above bounding functions (41) and (42) will be specified in the next subsection. Here we only use f_L and f_U to introduce the BnB framework for notational convenience. In the BnB algorithm, we store all the subproblems in a problem set $\mathcal{S}$, which will be updated together with the global bounds in each iteration by the following rules [57]

1) **Branching**: Pick a problem $\mathcal{P}(\Theta) \in \mathcal{S}$ that yields the smallest lower-bound. Equally divide Θ into two subregions following some subdivision rules detailed in the following, and generate two subproblems. Then delete $\mathcal{P}(\Theta)$ in the problem set.
2) **Pruning** (optional): Evaluate the qualification of the two subproblems. If their lower-bounds are less than the current global upper-bound, add them into $\mathcal{S}$.
3) **Bounding**: Choose the smallest lower-bound and upper-bound from $\mathcal{S}$ as the bounds for the next iteration.

Note that the pruning step is only for saving the memory of storing $\mathcal{S}$, and will not affect the effectiveness of the BnB procedure. This is because by choosing the smallest bounds in $\mathcal{S}$ we can always avoid the unqualified branches. For clarity, we summarize our BnB algorithm in Algorithm 3.

Algorithm 3: Branch-and-Bound Method for Solving (36).

Input: $\tilde{\mathbf{H}}, \mathbf{S}, \mathbf{x}_0, 0 \le \varepsilon \le 2$, tolerance threshold $\delta > 0$, bound functions f_L and f_U.
Initialization: Let Θ_0 be the initial feasible region of problem (27), $\mathcal{S} = \{\mathcal{P}(\Theta_0), f_U(\Theta_0), f_L(\Theta_0)\}$ be the initialized subproblem set. Set $UB = f_U(\Theta_0)$, $LB = f_L(\Theta_0)$.
while $UB - LB > \delta$ **do**
Branching
a) Pick $\mathcal{P}(\Theta) \in \mathcal{S}$, such that $f_L(\Theta) = LB$. Update $\mathcal{S} = \mathcal{S} \backslash \mathcal{P}(\Theta)$.
b) Divide Θ into Θ_A and Θ_B following the chosen subdivision rule.
Bounding
a) Compute $f_U(\Theta_i)$ and $f_L(\Theta_i)$ for $\mathcal{P}(\Theta_i), i = A, B$, and add them to $\mathcal{S}$.
b) Update UB and LB as the smallest upper-bound and lower-bound in $\mathcal{S}$, respectively.
end while
Output: $\mathbf{x}_{opt}$ = the feasible solution that achieves UB.

To ensure that Algorithm 3 converges in a finite number of iterations, the chosen subproblem for branching, the subdivision rule and the bounding functions f_L and f_U should satisfy the following conditions [57]

1) The branching is bounding-improving, i.e., in each iteration we choose the problem that yields the smallest lower-bound as the branching node.
2) The subdivision is exhaustive, i.e., the maximum length of the subregions converges to zero as the iteration number goes to infinity.
3) The bounding is consistent with branching, i.e., $UB - f_{opt}$ converges to zero as the maximum length of the

subregions goes to zero, where f_{opt} is the optimal value of the original problem.

Our Algorithm 3 satisfies condition 1) automatically. We then choose the subdivision rules to obtain the subproblems from the branching node. For a given node $\mathcal{P}(\Theta)$, we consider the following two rules:

- **Basic rectangular subdivision** (BRS): Equally divide Θ along $arc(l_n, u_n)$ and keep $arc(l_i, u_i), \forall i \neq n$ unchanged, where

$$n = \arg\max_n \{\phi_n \,|\phi_n = u_n - l_n\}. \tag{43}$$

- **Adaptive rectangular subdivision** (ARS): Equally divide Θ along $arc(l_n, u_n)$ and keep $arc(l_i, u_i), \forall i \neq n$ unchanged, where

$$n = \arg\max_n \{d_n \,|d_n = |x_u(n) - x_l(n)|\}. \tag{44}$$

In (44) $\mathbf{x}_u$ and $\mathbf{x}_l$ are the solutions associated with $f_U(\Theta)$ and $f_L(\Theta)$, respectively.

According to [57, Theorem 6.3 and 6.4], both the above two rules satisfy condition 2). In practical simulations, we observe that ARS has a faster convergence rate than BRS.

C. Upper-bound and Lower-bound Acquisition

It remains to develop approaches to acquire the lower and upper bounds, which are key to accelerating the BnB procedure. Following the approach in [58], we compute the lower-bound by the convex relaxation of (40). As shown in Fig. 2, the convex hull for each entry $x(n)$, denoted as $\mathcal{Q}(\theta_n)$, is a circular segment, and can be given as

$$\mathcal{Q}(\theta_n) : \{x \,|\arg(x) \in \theta_n, |x| \leq 1\}. \tag{45}$$

By simple analytic geometry, the angle constraint can be equivalently written as

$$\mathrm{Re}\left(x^* \left(\frac{e^{ju} + e^{jl}}{2}\right)\right) \geq \cos\left(\frac{u-l}{2}\right), \tag{46}$$

which is nothing but a linear constraint. It follows that the constraint for the vector variable is

$$\mathrm{Re}\left(\mathbf{x}^* \circ \left(\frac{e^{j\mathbf{u}} + e^{j\mathbf{l}}}{2}\right)\right) \geq \cos\left(\frac{\mathbf{u}-\mathbf{l}}{2}\right), \tag{47}$$

where $\mathbf{u} = [u_1, u_2, \ldots, u_N]^T \in \mathbb{R}^{N\times 1}, \mathbf{l} = [l_1, l_2, \ldots, l_N]^T \in \mathbb{R}^{N\times 1}$, and $\circ$ denotes the Hadamard product. Hence, the convex relaxation can be given as the following QCQP problem

$$\text{QP-LB}: \min_{\mathbf{x}} \ \|\mathbf{H}\mathbf{x} - \mathbf{s}\|^2 \tag{48a}$$

$$s.t. \ \mathrm{Re}\left(\mathbf{x}^* \circ \left(\frac{e^{j\mathbf{u}} + e^{j\mathbf{l}}}{2}\right)\right) \geq \cos\left(\frac{\mathbf{u}-\mathbf{l}}{2}\right), \tag{48b}$$

$$|x(n)|^2 \leq 1, \forall n. \tag{48c}$$

Problem (48) can be efficiently solved via numerical solvers, e.g., the CVX toolbox. By doing so, we can readily obtain the lower-bound for each subproblem.

A natural way to compute the upper-bound is to project each entry of the obtained solution $\mathbf{x}_l$ of (48) on the corresponding arc to get a feasible solution. Such a projector can be given in an element-wise manner as follows

$$\mathrm{PR}_1(x) = \begin{cases} x/|x|, \arg\ x \in [l, u], \\ \exp(jl), \arg\ x \in [(l+u)/2 + \pi, l + 2\pi], \\ \exp(ju), \arg\ x \in [u, (l+u)/2 + \pi], \end{cases} \tag{49}$$

where we omit the subscripts for convenience.

The upper-bound obtained by the projector (49) is still loose in general. To get a tighter bound, one can use $\mathrm{PR}_1(\mathbf{x}_l)$ as the initial point, and solve the following non-convex QCQP

$$\text{QP-UB}: \min_{\mathbf{x}} \ \|\mathbf{H}\mathbf{x} - \mathbf{s}\|^2 \tag{50a}$$

$$s.t. \ \mathrm{Re}\left(\mathbf{x}^* \circ \left(\frac{e^{j\mathbf{u}} + e^{j\mathbf{l}}}{2}\right)\right) \geq \cos\left(\frac{\mathbf{u}-\mathbf{l}}{2}\right), \tag{50b}$$

$$|x(n)|^2 = 1, \forall n. \tag{50c}$$

which can be locally solved via the *fmincon* solver in MATLAB. Since the solver employs descent methods, the obtained local minimizer is guaranteed to yield a smaller value than $f(\mathrm{PR}_1(\mathbf{x}_l))$.

To further accelerate the speed for solving QP-LB and obtaining the bounds, we consider accelerated gradient projection (GP) methods [59] in addition to the QCQP solvers. Given $x_n \in \mathbb{C}$, the projector PR_2 projects x_n to the nearest point in the corresponding convex hull $\mathcal{Q}(\theta_n)$. The details for deriving PR_2 are provided in Appendix A. Here we briefly introduce our iterative scheme as

$$\mathbf{v} = \mathbf{x}^{(k)} + \frac{k-1}{k+2}\left(\mathbf{x}^{(k)} - \mathbf{x}^{(k-1)}\right), \tag{51}$$

$$\mathbf{x}^{(k+1)} = \mathrm{PR}_2\left(\mathbf{v} - 2s\tilde{\mathbf{H}}^H\left(\tilde{\mathbf{H}}\mathbf{v} - \mathbf{s}\right)\right), \tag{52}$$

where we start from $\mathbf{x}^{(0)}$ and $\mathbf{x}^{(1)} = \mathbf{x}^{(0)}$. For the least-squares objective function, we choose the stepsize as $s = 1/\tilde{\lambda}_{\max}$, where $\tilde{\lambda}_{\max}$ is the maximum eigenvalue of $\tilde{\mathbf{H}}^H\tilde{\mathbf{H}}$, i.e., the Lipschitz constant.

Note that the above iteration scheme can only be used for convex feasible regions due to the interpolation operation (51). For the non-convex QP-UB problem (50), we use $\mathbf{x}^{(k)}$ instead of the interpolated point $\mathbf{v}$, and replace the projector PR_2 with PR_1, which projects the point onto the arc, i.e., the feasible region. Similar to (50), we use $\mathrm{PR}_1(\mathbf{x}_l)$ as the initial point.

Based on [60], the complexity for using interior-point method to solve the QCQP problems is $\mathcal{O}(N^3)$ per iteration. For both gradient-based methods, the costs are $\mathcal{O}(NK)$ in each iteration, which are far more efficient in terms of a fixed iteration number.

D. Convergence Analysis and Worst-case Complexity

We end this section by analyzing the convergence behavior and the worst-case complexity for the proposed Algorithm 3. The convergence proof is to show that our bounding functions f_L and f_U satisfy the condition 3). Recall the definitions of ϕ_n and

d_n in (43) and (44). By denoting $\phi_{\max} = \max\{\phi_n\}, d_{\max} = \max\{d_n\}$, we have the following Lemma 1.

Lemma 1: As $\phi_{\max}$ or $d_{\max}$ goes to zero, the difference between UB and LB uniformly converges to zero, i.e.,

$$\forall \delta > 0, \exists \eta_1, \eta_2 \geq 0 \;\; s.t.$$
$$\phi_{\max} \leq \eta_1 \;\; or \;\; d_{\max} \leq \eta_2 \Rightarrow UB - LB \leq \delta. \tag{53}$$

Proof: See Appendix B. ■

Theorem 1: Algorithm 3 converges in a finite number of iterations to a value arbitrarily close to f_{opt}.

Proof: See Appendix C. ■

The following Theorem 2 specifies the worst-case complexity of Algorithm 3 for using BRS.

Theorem 2: When the BRS is used, Algorithm 3 converges to a δ-optimal solution for at most

$$T = \left\lceil \frac{2^{N+1} \arccos^N\left(1 - \varepsilon^2/2\right)}{\eta_1} \right\rceil \tag{54}$$

iterations, where η_1 is given by (67) in Appendix B.

Proof: See Appendix D. ■

Although the worst-case costs of both BnB-ARS and BnB-BRS are at the exponential order with N, our simulations show that in most cases, the algorithm terminates at a small iteration number thanks to the tight bounds.

VI. Numerical Results

In this section, we present numerical results to validate the effectiveness of the proposed waveform design approaches. For convenience, we set $P_T = 1$, and each entry of the channel matrix $\mathbf{H}$ subject to standard Complex Gaussian distribution, i.e., $h_{i,j} \sim \mathcal{CN}(0,1)$. In all the simulations, we set $N = 16$ and employ a ULA with half-wavelength spacing between the adjacent antennas. The constellation chosen for the communication users is the unit-power QPSK alphabet, i.e., the power of each entry in the symbol matrix $\mathbf{S}$ is 1. Without loss of generality, we define $\mathrm{SNR} = P_T/N_0$, and use 'Omni' and 'Directional' to represent omnidirectional and directional beampattern designs. Further, we denote the waveform optimizations with strict equality constraints and the trade-off designs as 'Strict' and 'Tradeoff', and use 'Total' and 'perAnt' for the total and per-antenna power constrained optimizations, i.e., (16) and (26), respectively. The length of the communication frame/radar pulse is set as $L = 30$.

A. Dual-functional Waveform Design with Given Radar Beampatterns

We first show the communication performance obtained by different approaches in Fig. 3 and Fig. 4 in terms of the sum-rate and the symbol error rate (SER), while the associated radar beampatterns are given in Fig. 5. For directional beampattern design, we consider three targets of interest with angles of $-\pi/3, 0$ and $\pi/3$, and exploit the classic LS techniques [43] to obtain the desired covariance matrix $\mathbf{R}_d$ as defined in (10). It can be observed in Fig. 3 and Fig. 4 that, the proposed omnidirectional designs always outperform the directional ones in terms

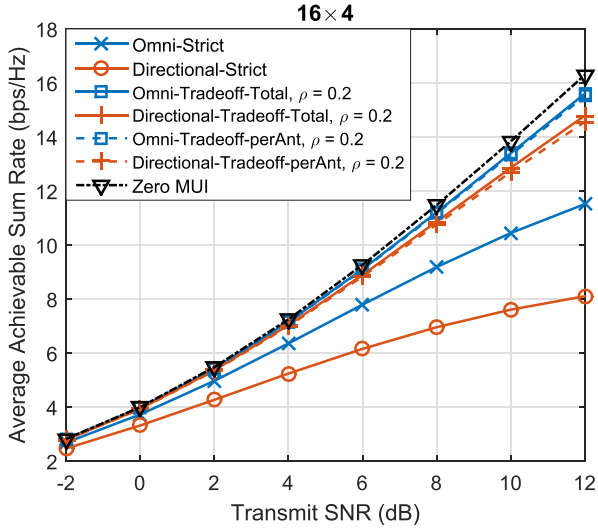

Fig. 3. Sum-rate comparison for different approaches, $N = 16, K = 4$.

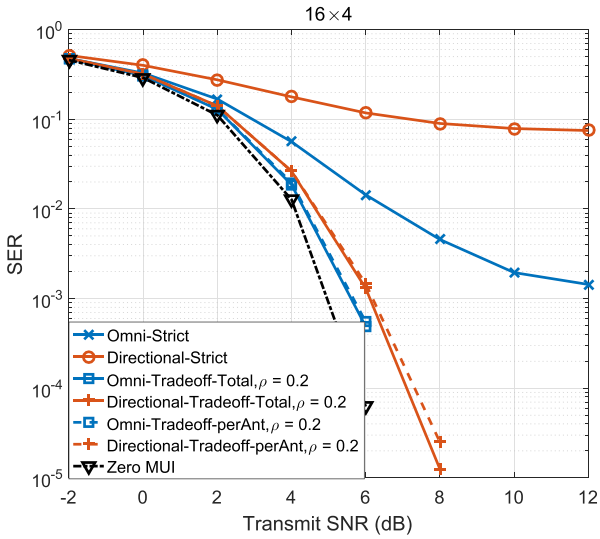

Fig. 4. Symbol error rate comparison for different approaches, $N = 16$, $K = 4$.

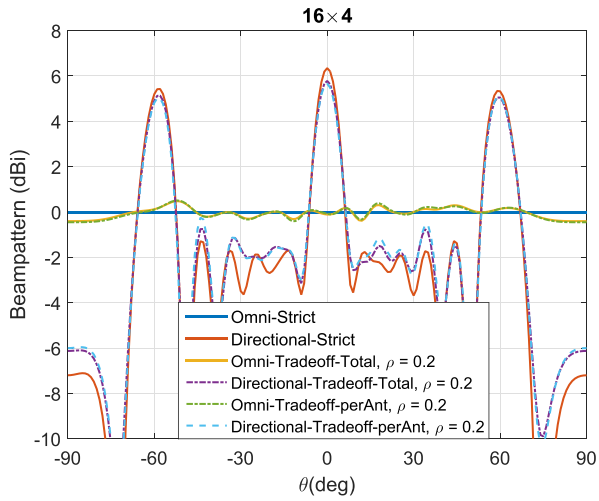

Fig. 5. Radar beampatterns obtained by different approaches, $N = 16$, $K = 4$.

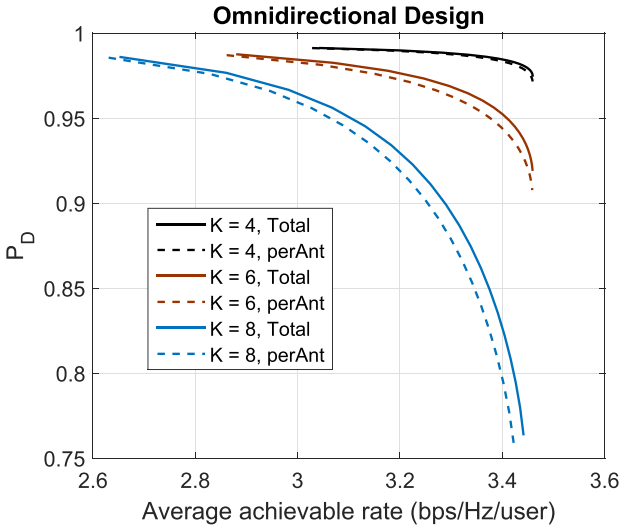

Fig. 6. Trade-off between the achievable rate per user and the radar detection probability for omnidirectional beampattern design, $N = 16$, radar SNR $= -6$ dB, $P_{FA} = 10^{-7}$.

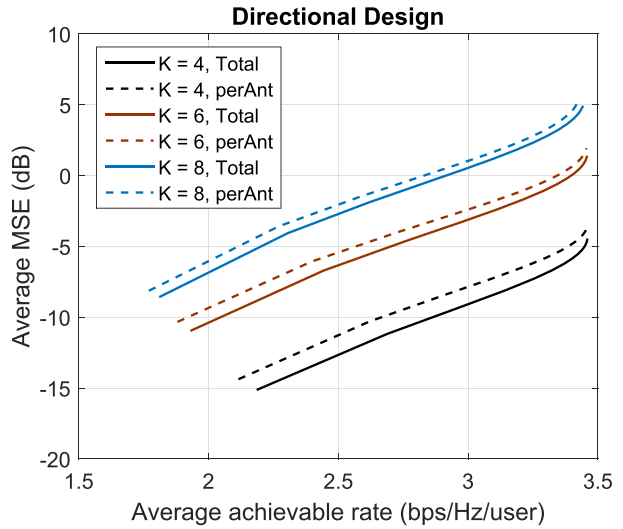

Fig. 7. Trade-off of the achievable rate per user and the average MSE between the designed and desired directional beampattern, $N = 16$.

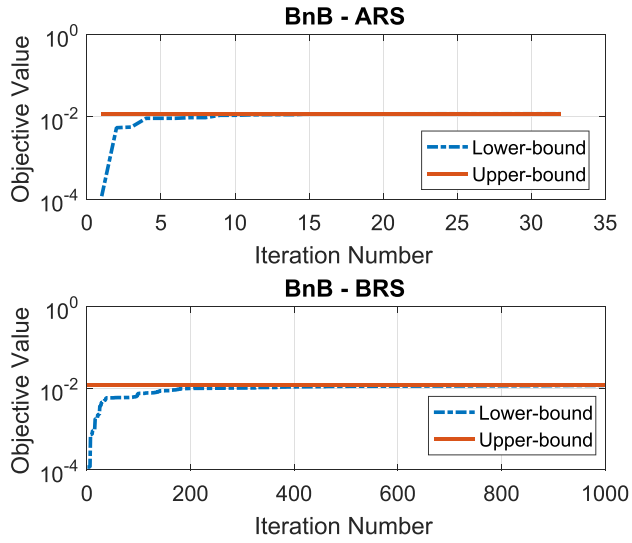

Fig. 8. Convergence Behavior of BnB Algorithm for $N = 16$, $K = 4$, $\varepsilon = 1$.

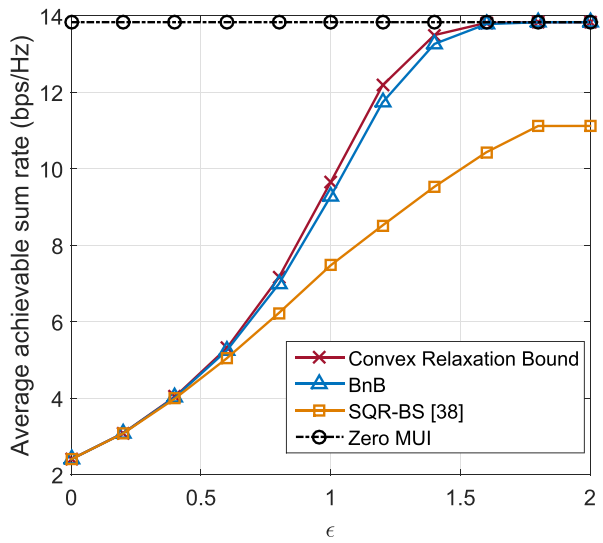

Fig. 9. Trade-off between the communication sum-rate and radar waveform similarity, $N = 16$, $K = 4$, SNR $= 10$ dB.

of both the sum-rate and the SER. The resultant radar beampatterns are shown in Fig. 5 for 'Strict', which are exactly the same with the desired beampatterns. Moreover, by introducing a small weighting factor $\rho = 0.2$ to the communication side, the sum-rates as well as the SER performance for trade-off designs improve significantly by approaching to that of the zero MUI cases, i.e., the performance lower-bounds. Meanwhile in Fig. 5, the corresponding radar beampatterns only experience slight performance loss. By further looking at the per-antenna power constrained designs, we see that the corresponding performance losses in either radar or communication are negligible in contrast with their total power constrained counterparts, which suggests that the proposed RCG algorithm can effectively yield near-optimal solutions to the non-convex problem (26).

In Fig. 6 and 7, we aim to explicitly show the trade-offs between the communication and radar performance. For omnidirectional beampattern design, the detection probability P_D is used as the metric, where we consider the constant false-alarm rate (CFAR) detection for a point-like target in the far field, located at the angle of $\pi/5$. The receive SNR is fixed at -6 dB. The false-alarm probability for radar is $P_{FA} = 10^{-7}$. We calculate the detection probability based on [9, eq. (69)]. It can be seen that there exists a trade-off between the communication rate and the radar detection performance. For a fixed P_D, the achievable rate increases with the decrease of the number of users, which suggests that the MUI energy can be further minimized by increasing the DoFs. Again, by replacing the total power constraint as per-antenna ones, the associated performance only decreases marginally. The same trends appear in Fig. 6 for the directional beampattern, where we employ the mean squared error (MSE) between the desired and obtained

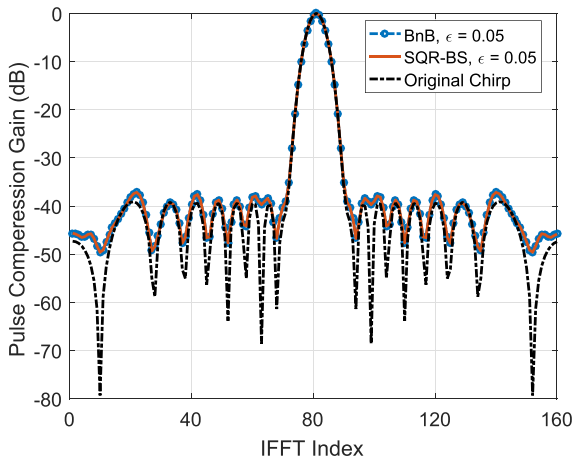

(a)

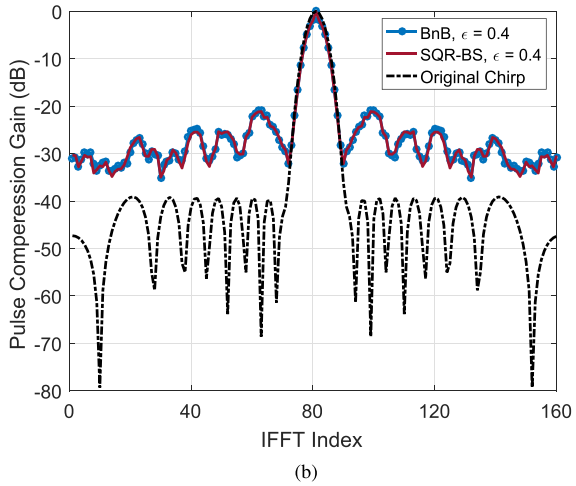

(b)

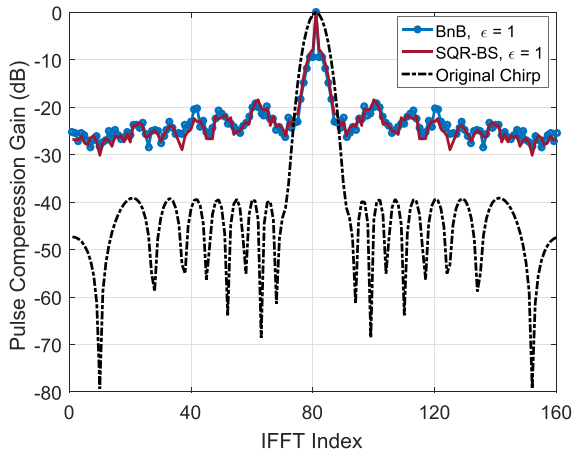

(c)

Fig. 10. Radar pulse compression for different similarity tolerance, $N = 16, K = 4$. (a) $\varepsilon = 0.05$; (b) $\varepsilon = 0.4$; (c) $\varepsilon = 1$.

directional beampatterns as the radar metric. Both figures prove that our approach can achieve a favorable trade-off between radar and communications.

B. Dual-functional Constant Modulus Waveform Design

We show the results for solving the waveform optimization problem with CMC and SC in Figs. 8–10. Following the simulation configurations in [38], we employ the orthogonal chirp waveform matrix as the reference signal. The convergence behavior of the proposed BnB algorithm for solving (36) is shown in Fig. 8, with $N = 16, K = 4, \varepsilon = 1$, where we compare the performance of the two different subdivision rules, i.e., ARS and BRS. Both methods converge in a finite number of iterations with a nearly constant upper-bound, which suggests that we can reach the optimal value of problem (36) by iteratively using the local algorithms for several times, e.g., QCQP solver or the proposed gradient projection method. Nevertheless, due to the non-convexity of the problem, we need BnB algorithm to confirm that this is indeed a global optimum. It can be also observed that the BnB-ARS has a faster convergence rate than BnB-BRS, which is consistent with the analysis in [57].

In Fig. 9 and 10, we show the trade-off between communication sum-rate and radar waveform similarity for the constant modulus designs, where we employ the SQR-Binary Search (SQR-BS) algorithm proposed by [38] as our benchmark technique. Fig. 9 demonstrates the communication sum-rate with increasing ε for $N = 16, K = 4, \mathrm{SNR} = 10$ dB. As expected, the proposed BnB algorithm outperforms the SQR-BS significantly, since the result obtained by BnB is the global optimum, while SQR-BS can only yield local minimum solutions. It is worth highlighting that the performance of BnB is very close to the convex relaxation bound, which is obtained by solving QP-LB. When the similarity tolerance ε is big enough, our BnB algorithm can approximate the zero MUI performance.

Fig. 10 shows the results of radar pulse compression with different similarity tolerance ε, where we use the waveform transmitted by the first antenna, and employ the classic FFT-IFFT pulse compression method [61] with a Taylor window to reduce the power of sidelobes. From Fig. 9–10 we see that there exists a trade-off between the communication sum-rate and radar pulse compression performance. Moreover, the pulse compression results of BnB and SQR-BS are nearly the same, as their performance is guaranteed by the same waveform similarity constraint, which again proves the superiority of the proposed BnB Algorithm.

VII. Conclusion

In this paper, we have discussed the waveform design for dual-functional radar-communication system, used for simultaneous target detection and downlink communications. First of all, we have proposed two design approaches to minimize the multi-user interference while formulating an appropriate radar beampattern. We have further designed the dual-functional waveforms via weighted optimizations under both total and per-antenna power constraints, which achieve a flexible performance trade-off between the radar and the communication. It has been proven that the computational costs for most of the above methods are at the same level with the communication-only ZF precoding. Numerical results have shown that the proposed approaches guarantee both the radar and the communication performance. Moreover, our trade-off designs can significantly improve the communication performance by allowing a slight performance loss at radar. Finally, we have considered non-convex constant modulus waveform design with similar-

ity constraints, where an efficient global optimization algorithm based on the branch-and-bound framework has been developed. Gradient projection algorithms have been developed to efficiently obtain the upper and lower bounds. Simulations have shown that the proposed BnB algorithm for constant modulus waveform design with similarity constraints considerably outperforms the conventional SQR-BS algorithm by obtaining the global optimum of the problem.

Future research will focus on waveform designs with further practical radar metrics, such as auto-correlation and cross-correlation constraints, which are important to the target detection performance. Moreover, since the computational costs of the proposed closed-form waveform designs (8), (10) and the trade-off design (16) are rather low, it is easy to implement them on a hardware platform, which can further prove the effectiveness of the proposed methods in realistic scenarios.

APPENDIX A
DERIVATION OF THE PROJECTOR PR_2

The projector is derived for two cases respectively, i.e., the open angle of the circular segment is (a) less than π or (b) greater than π. We start from the first case. As shown in Fig. 11(a), the whole complex plane $\mathbb{C}$ has been divided into five parts. The lower and the upper bounds for the angle are l and u respectively. Let us define

$$A = \exp(jl), B = \exp(ju), T = (A+B)/2, \tag{55}$$

where T is the midpoint of AB. Given $X \in \mathbb{C}$, we aim to find a nearest point $\mathrm{PR}_2(X) \in M_1$ as the projection. Note that $\forall X \in M_1$, the projection is itself. For $X \in M_2$ and $X \in M_3$, the nearest points are A and B respectively. For $X \in M_4$, we project it onto the line AB, and the projection is the foot of perpendicular. For $\forall X \in M_5 = \mathbb{C} \backslash \bigcup_{i=1}^{4} M_i$, we use the normalization as its projection. By basic plane analytic geometry, we define the following lines

$$\begin{aligned}
&\text{Line } AB: \quad f_1(X) = \mathrm{Re}\left(T^*(X-T)\right) = 0,\\
&\text{Line } OA: \quad f_2(X) = -\mathrm{Re}\left(jA^*X\right) = 0,\\
&\text{Line } OB: \quad f_3(X) = \mathrm{Re}\left(jB^*X\right) = 0,\\
&\text{Line } AQ: \quad f_4(X) = \mathrm{Re}\left((A-B)^*(X-A)\right) = 0,\\
&\text{Line } BP: \quad f_5(X) = \mathrm{Re}\left((B-A)^*(X-B)\right) = 0.
\end{aligned} \tag{56}$$

The projector is then given as

$$\mathrm{PR}_2(X) = \begin{cases} X, \ f_1(X) \geq 0, \ |X| \leq 1 \ (X \in M_1), \\ A, \ \ f_2(X) \leq 0 \leq f_4(X) \ (X \in M_2), \\ B, \ \ f_3(X) \leq 0 \leq f_4(X) \ (X \in M_3), \\ X_T, f_1(X), f_4(X), f_5(X) \leq 0 \ (X \in M_4), \\ X/|X|, \ \text{else}, \end{cases} \tag{57}$$

where X_T is the foot of perpendicular on AB, i.e., $XX_T \perp AB, X_T \in AB$. This is given by

$$X_T = X - \mathrm{Re}\left((X-T)^*T\right)\frac{T}{|T|}. \tag{58}$$

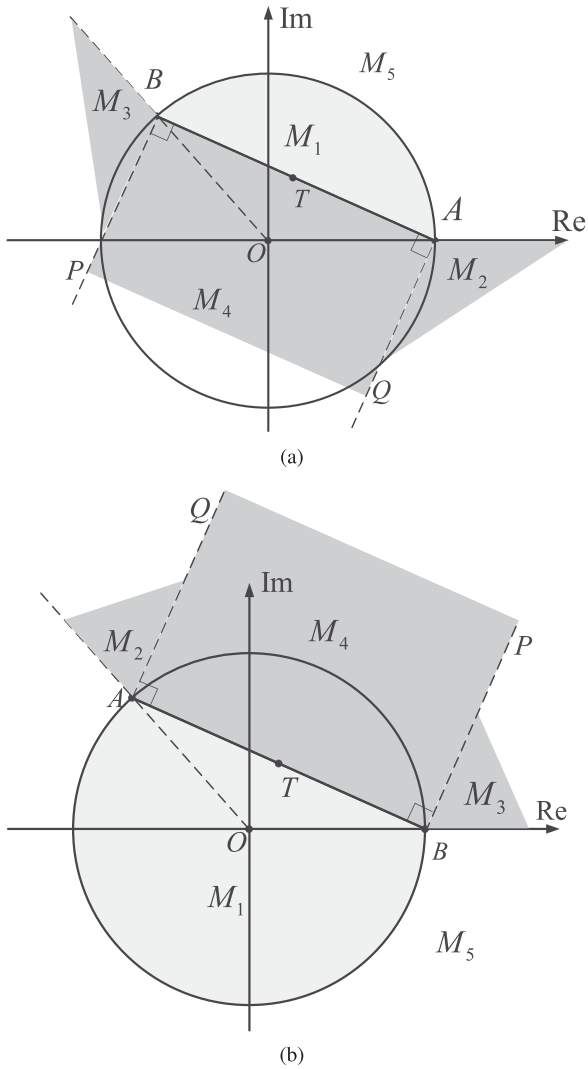

Fig. 11. Projector for GP. (a) $\phi \leq \pi$; (b) $\phi \geq \pi$.

For the case of $\phi \geq \pi$ the projector is the same. The only difference is that $f_1(X)$ should be defined as

$$f_1(X) = -\mathrm{Re}\left(T^*(X-T)\right). \tag{59}$$

APPENDIX B
PROOF OF LEMMA 1

Let us first denote the points that generate UB and LB as $\mathbf{x}_u$ and $\mathbf{x}_l$, i.e., $UB = f(\mathbf{x}_u), LB = f(\mathbf{x}_l)$. Following the Lagrange Mean-value Theorem we have

$$\begin{aligned}
UB - LB &= f(\mathbf{x}_u) - f(\mathbf{x}_l)\\
&= \nabla f^H(\mathbf{z})(\mathbf{x}_u - \mathbf{x}_l)\\
&\leq \|\nabla f(\mathbf{z})\| \, \|(\mathbf{x}_u - \mathbf{x}_l)\|,
\end{aligned} \tag{60}$$

where

$$\mathbf{z} \in \{\mathbf{w} \,|\mathbf{w} = t\mathbf{x}_u + (1-t)\mathbf{x}_l, t \in [0,1]\}. \tag{61}$$

The upper-bound of the gradient is given as

$$\begin{aligned}\|\nabla f(\mathbf{z})\| &= 2\left\|\tilde{\mathbf{H}}^H\left(\tilde{\mathbf{H}}\mathbf{z}-\mathbf{s}\right)\right\| \\ &\le 2\left\|\tilde{\mathbf{H}}^H\tilde{\mathbf{H}}\mathbf{z}\right\| + 2\left\|\tilde{\mathbf{H}}^H\mathbf{s}\right\| \\ &\le 2\sqrt{N}\tilde{\lambda}_{\max} + 2\left\|\tilde{\mathbf{H}}^H\mathbf{s}\right\|, \end{aligned} \tag{62}$$

where the second line of (62) is based on the triangle inequality, the third line is based on the definition of the matrix l_2 norm.

For the convex hull of each $\mathrm{arc}\,(l_n, u_n)$, the longest line segment is the chord shown in Fig. 2 ($\phi_n \le \pi$) or the diameter ($\phi_n \ge \pi$). By simple geometric relations we have

$$\|\mathbf{x}_u - \mathbf{x}_l\| \le \sqrt{N} d_{\max} \le 2\sqrt{\sum_{n=1}^{N} \sin^2\left(\frac{\min(\phi_n, \pi)}{2}\right)}. \tag{63}$$

For $\phi_n \le \pi, \forall n$, it follows that

$$\|\mathbf{x}_u - \mathbf{x}_l\| \le \sqrt{N} d_{\max} \le 2\sqrt{N}\sin\left(\frac{\phi_{\max}}{2}\right). \tag{64}$$

By using (60), (62) and (64) we obtain

$$UB - LB \le 4\left(N\tilde{\lambda}_{\max} + \sqrt{N}\left\|\tilde{\mathbf{H}}^H\mathbf{s}\right\|\right)\sin\left(\frac{\phi_{\max}}{2}\right), \tag{65}$$

$$UB - LB \le 2\left(N\tilde{\lambda}_{\max} + \sqrt{N}\left\|\tilde{\mathbf{H}}^H\mathbf{s}\right\|\right) d_{\max}. \tag{66}$$

Given any $\delta > 0$, let

$$\eta_1 = \min\left(\pi, 2\arcsin\left(\frac{\delta}{4\left(N\tilde{\lambda}_{\max} + \sqrt{N}\left\|\tilde{\mathbf{H}}^H\mathbf{s}\right\|\right)}\right)\right), \tag{67}$$

$$\eta_2 = \frac{\delta}{2\left(N\tilde{\lambda}_{\max} + \sqrt{N}\left\|\tilde{\mathbf{H}}^H\mathbf{s}\right\|\right)}, \tag{68}$$

we have $UB - LB \le \delta$ if $\phi_{\max} \le \eta_1$ or $d_{\max} \le \eta_2$.

Appendix C
Proof of Theorem 1

Algorithm 2 satisfies both conditions 1) and 2). Furthermore, according to the definition of UB and LB we have

$$0 \le UB - f_{opt} \le UB - LB. \tag{69}$$

According to Lemma 1, the bounding is consistent with branching for the proposed two subdivision rules. Therefore, Algorithm 2 satisfies condition 3), which completes the proof.

Appendix D
Proof of Theorem 2

Define $\mathrm{vol}\,(\Theta_0) = \left(2\arccos\left(1-\varepsilon^2/2\right)\right)^N$ as the volume of the initialized feasible region. Assume that Algorithm 2 terminates at the *T*-th iteration. According to [62], we have

$$\frac{\phi_{\max}}{2} \le \frac{\mathrm{vol}\,(\Theta_0)}{T} \le \frac{\eta_1}{2}, \tag{70}$$

where η_1 is defined by (67). It follows that

$$T \ge \frac{2\,\mathrm{vol}\,(\Theta_0)}{\eta_1} = \frac{2^{N+1}\arccos^N\left(1-\varepsilon^2/2\right)}{\eta_1}, \tag{71}$$

which completes the proof.

References

[1] FCC. Connecting America: The national broadband plan. 2010. [Online]. Available: https://www.fcc.gov/general/national-broadband-plan

[2] NSF. Enhancing access to the radio spectrum (EARS). 2013. [Online]. Available: https://www.nsf.gov/pubs/2013/nsf13539/nsf13539.htm

[3] DARPA. Shared spectrum access for radar and communications (SSPARC). 2016. [Online]. Available: http://www.darpa.mil/program/shared-spectrum-access-for-radar-and-commu%nications

[4] NSF. Spectrum efficiency, energy efficiency, and security (SpecEES): Enabling spectrum for all. 2016. [Online]. Available: https://www.nsf.gov/pubs/2016/nsf16616/nsf16616.htm

[5] Ofcom. Public sector spectrum release: Award of the 2.3 and 3.4 GHz spectrum bands. 2015. [Online]. Available: https://www.ofcom.org.uk/consultations-and-statements/category-1/2.3-3.%4-ghz-auction-design

[6] ECC. The European table of frequency allocations and applocations in the frequency range 8.3 kHz to 3000 GHz (ECA table). 2016. [Online]. Available: http://www.erodocdb.dk/docs/doc98//official/pdf/ERCREP025.PDF

[7] R. Saruthirathanaworakun, J. M. Peha, and L. M. Correia, "Opportunistic sharing between rotating radar and cellular," *IEEE J. Sel. Areas Commun.*, vol. 30, no. 10, pp. 1900–1910, Nov. 2012.

[8] S. Sodagari, A. Khawar, T. C. Clancy, and R. McGwier, "A projection based approach for radar and telecommunication systems coexistence," in *Proc. IEEE Global Commun. Conf.*, Dec. 2012, pp. 5010–5014.

[9] A. Khawar, A. Abdelhadi, and C. Clancy, "Target detection performance of spectrum sharing MIMO radars," *IEEE Sensors J.*, vol. 15, no. 9, pp. 4928–4940, Sep. 2015.

[10] J. A. Mahal, A. Khawar, A. Abdelhadi, and T. C. Clancy, "Spectral coexistence of MIMO radar and MIMO cellular system," *IEEE Trans. Aerosp. Electron. Syst.*, vol. 53, no. 2, pp. 655–668, Apr. 2017.

[11] A. Babaei, W. H. Tranter, and T. Bose, "A nullspace-based precoder with subspace expansion for radar/communications coexistence," in *Proc. IEEE Global Commun. Conf.*, Dec. 2013, pp. 3487–3492.

[12] B. Li and A. Petropulu, "MIMO radar and communication spectrum sharing with clutter mitigation," in *Proc. IEEE Radar Conf.*, May 2016, pp. 1–6.

[13] B. Li, A. P. Petropulu, and W. Trappe, "Optimum co-design for spectrum sharing between matrix completion based MIMO radars and a MIMO communication system," *IEEE Trans. Signal Process.*, vol. 64, no. 17, pp. 4562–4575, Sep. 2016.

[14] B. Li and A. Petropulu, "Joint transmit designs for co-existence of MIMO wireless communications and sparse sensing radars in clutter," *IEEE Trans. Aerosp. Electron. Syst.*, vol. 53, no. 6, pp. 2846–2864, Dec. 2017.

[15] L. Zheng, M. Lops, X. Wang, and E. Grossi, "Joint design of overlaid communication systems and pulsed radars," *IEEE Trans. Signal Process.*, vol. 66, no. 1, pp. 139–154, Jan. 2018.

[16] L. Zheng, M. Lops, and X. Wang, "Adaptive interference removal for uncoordinated radar/communication coexistence," *IEEE J. Sel. Topics Signal Process.*, vol. 12, no. 1, pp. 45–60, Feb. 2018.

[17] F. Liu, C. Masouros, A. Li, and T. Ratnarajah, "Robust MIMO beamforming for cellular and radar coexistence," *IEEE Wireless Commun. Lett.*, vol. 6, no. 3, pp. 374–377, Jun. 2017.

[18] F. Liu, C. Masouros, A. Li, T. Ratnarajah, and J. Zhou, "MIMO radar and cellular coexistence: A power-efficient approach enabled by interference exploitation," *IEEE Trans. Signal Process.*, vol. 66, no. 14, pp. 3681–3695, Jul. 2018.

[19] A. R. Chiriyath, B. Paul, G. M. Jacyna, and D. W. Bliss, "Inner bounds on performance of radar and communications co-existence," *IEEE Trans. Signal Process.*, vol. 64, no. 2, pp. 464–474, Jan. 2016.

[20] A. R. Chiriyath, B. Paul, and D. W. Bliss, "Radar-communications convergence: Coexistence, cooperation, and co-design," *IEEE Trans. Cogn. Commun. Netw.*, vol. 3, no. 1, pp. 1–12, Mar. 2017.

[21] S. D. Blunt, P. Yatham, and J. Stiles, "Intrapulse radar-embedded communications," *IEEE Trans. Aerosp. Electron. Syst.*, vol. 46, no. 3, pp. 1185–1200, Jul. 2010.

[22] S. D. Blunt, J. G. Metcalf, C. R. Biggs, and E. Perrins, "Performance characteristics and metrics for intra-pulse radar-embedded communication," *IEEE J. Sel. Areas Commun.*, vol. 29, no. 10, pp. 2057–2066, Dec. 2011.
[23] D. Ciuonzo, A. De Maio, G. Foglia, and M. Piezzo, "Intrapulse radar-embedded communications via multiobjective optimization," *IEEE Trans. Aerosp. Electron. Syst.*, vol. 51, no. 4, pp. 2960–2974, Oct. 2015.
[24] G. N. Saddik, R. S. Singh, and E. R. Brown, "Ultra-wideband multifunctional communications/radar system," *IEEE Trans. Microw. Theory Techn.*, vol. 55, no. 7, pp. 1431–1437, Jul. 2007.
[25] C. Sturm and W. Wiesbeck, "Waveform design and signal processing aspects for fusion of wireless communications and radar sensing," *Proc. IEEE*, vol. 99, no. 7, pp. 1236–1259, Jul. 2011.
[26] J. Moghaddasi and K. Wu, "Multifunctional transceiver for future radar sensing and radio communicating data-fusion platform," *IEEE Access*, vol. 4, pp. 818–838, 2016.
[27] A. Hassanien, M. G. Amin, Y. D. Zhang, and F. Ahmad, "Dual-function radar-communications: Information embedding using sidelobe control and waveform diversity," *IEEE Trans. Signal Process.*, vol. 64, no. 8, pp. 2168–2181, Apr. 2016.
[28] A. Hassanien, M. G. Amin, Y. D. Zhang, and F. Ahmad, "Phase-modulation based dual-function radar-communications," *IET Radar Sonar Navig.*, vol. 10, no. 8, pp. 1411–1421, 2016.
[29] E. BouDaher, A. Hassanien, E. Aboutanios, and M. G. Amin, "Towards a dual-function MIMO radar-communication system," in *Proc. IEEE Radar Conf.*, May 2016, pp. 1–6.
[30] F. Liu, C. Masouros, A. Li, H. Sun, and L. Hanzo, "MU-MIMO communications with MIMO radar: From co-existence to joint transmission," *IEEE Trans. Wireless Commun.*, vol. 17, no. 4, pp. 2755–2770, Apr. 2018.
[31] V. Mancuso and S. Alouf, "Reducing costs and pollution in cellular networks," *IEEE Commun. Mag.*, vol. 49, no. 8, pp. 63–71, Aug. 2011.
[32] S. K. Mohammed and E. G. Larsson, "Per-antenna constant envelope precoding for large multi-user MIMO systems," *IEEE Trans. Commun.*, vol. 61, no. 3, pp. 1059–1071, Mar. 2013.
[33] J. C. Chen, "Low-PAPR precoding design for massive multiuser MIMO systems via Riemannian manifold optimization," *IEEE Commun. Lett.*, vol. 21, no. 4, pp. 945–948, Apr. 2017.
[34] P. V. Amadori and C. Masouros, "Constant envelope precoding by interference exploitation in phase shift keying-modulated multiuser transmission," *IEEE Trans. Wireless Commun.*, vol. 16, no. 1, pp. 538–550, Jan. 2017.
[35] F. Liu, C. Masouros, P. V. Amadori, and H. Sun, "An efficient manifold algorithm for constructive interference based constant envelope precoding," *IEEE Signal Process. Lett.*, vol. 24, no. 10, pp. 1542–1546, Oct. 2017.
[36] A. De Maio, S. De Nicola, Y. Huang, Z.-Q. Luo, and S. Zhang, "Design of phase codes for radar performance optimization with a similarity constraint," *IEEE Trans. Signal Process.*, vol. 57, no. 2, pp. 610–621, Feb. 2009.
[37] G. Cui, H. Li, and M. Rangaswamy, "MIMO radar waveform design with constant modulus and similarity constraints," *IEEE Trans. Signal Process.*, vol. 62, no. 2, pp. 343–353, Jan. 2014.
[38] O. Aldayel, V. Monga, and M. Rangaswamy, "Successive QCQP refinement for MIMO radar waveform design under practical constraints," *IEEE Trans. Signal Process.*, vol. 64, no. 14, pp. 3760–3774, Jul. 2016.
[39] O. Aldayel, V. Monga, and M. Rangaswamy, "Tractable transmit MIMO beampattern design under a constant modulus constraint," *IEEE Trans. Signal Process.*, vol. 65, no. 10, pp. 2588–2599, May 2017.
[40] J. Li and P. Stoica, *MIMO Radar Signal Processing*. Hoboken, NJ, USA: Wiley, 2009.
[41] J. Li and P. Stoica, "MIMO radar with colocated antennas," *IEEE Signal Process. Mag.*, vol. 24, no. 5, pp. 106–114, Sep. 2007.
[42] P. Stoica, J. Li, and Y. Xie, "On probing signal design for MIMO radar," *IEEE Trans. Signal Process.*, vol. 55, no. 8, pp. 4151–4161, Aug. 2007.
[43] D. R. Fuhrmann and G. S. Antonio, "Transmit beamforming for MIMO radar systems using signal cross-correlation," *IEEE Trans. Aerosp. Electron. Syst.*, vol. 44, no. 1, pp. 171–186, Jan. 2008.
[44] T. Viklands, "Algorithms for the weighted orthogonal procrustes problem and other least squares problems," Ph.D. dissertation, Comput. Sci. Dept., Umea Univ., Umea, Sweden, 2008.
[45] S. Boyd and L. Vandenberghe, *Convex Optimization*. Cambridge, U.K.: Cambridge Univ. Press, 2004.
[46] A. Fradkov and V. Yakubovich, "The S-procedure and duality relations in nonconvex problems of quadratic programming," *Vestn. LGU, Ser. Mat. Mekh. Astron*, no. 1, pp. 101–109, 1979.
[47] R. J. Stern and H. Wolkowicz, "Indefinite trust region subproblems and nonsymmetric eigenvalue perturbations," *SIAM J. Optim.*, vol. 5, no. 2, pp. 286–313, 1995.
[48] C. Fortin and H. Wolkowicz, "The trust region subproblem and semidefinite programming," *Optim. Methods Softw.*, vol. 19, no. 1, pp. 41–67, 2004.
[49] F. Rendl and H. Wolkowicz, "A semidefinite framework for trust region subproblems with applications to large scale minimization," *Math. Program.*, vol. 77, no. 1, pp. 273–299, 1997.
[50] W. Huyer and A. Neumaier, "Global optimization by multilevel coordinate search," *J. Global Optim.*, vol. 14, no. 4, pp. 331–355, 1999.
[51] P.-A. Absil, R. Mahony, and R. Sepulchre, *Optimization Algorithms on Matrix Manifolds*. Princeton, NJ, USA: Princeton Univ. Press, 2009.
[52] N. Boumal, "Optimization and estimation on manifolds," Ph.D. dissertation, Dept. Math. Eng., Univ. Catholique Louvain, Louvain-la-Neuve, Belgium, Feb. 2014.
[53] S. E. Selvan *et al.*, "Descent algorithms on oblique manifold for source-adaptive ICA contrast," *IEEE Trans. Neural Netw. Learn. Syst.*, vol. 23, no. 12, pp. 1930–1947, Dec. 2012.
[54] P. Petersen, *Riemannian Geometry*, vol. 171. Berlin, Germany: Springer, 1998.
[55] L. Zhou, L. Zheng, X. Wang, W. Jiang, and W. Luo, "Coordinated multicell multicast beamforming based on manifold optimization," *IEEE Commun. Lett.*, vol. 21, no. 7, pp. 1673–1676, 2017.
[56] A. Cherian and S. Sra, "Riemannian dictionary learning and sparse coding for positive definite matrices," *IEEE Trans. Neural Netw. Learn. Syst.*, vol. 28, no. 12, Dec. 2017.
[57] H. Tuy, *Convex Analysis and Global Optimization*. Berlin, Germany: Springer, 2016.
[58] C. Lu and Y. F. Liu, "An efficient global algorithm for single-group multicast beamforming," *IEEE Trans. Signal Process.*, vol. 65, no. 14, pp. 3761–3774, Jul. 2017.
[59] Y. Nesterov, *Introductory Lectures on Convex Optimization: A Basic Course*. Norwell, MA, USA: Kluwer, 2004.
[60] M. S. Lobo, L. Vandenberghe, S. Boyd, and H. Lebret, "Applications of second-order cone programming," *Linear Algebra Appl.*, vol. 284, no. 1–3, pp. 193–228, 1998.
[61] M. A. Richards, J. Scheer, and W. A. Holm, *Principles of Modern Radar: Basic Principles*. New York, NY, USA: Scitech, 2010.
[62] S. K. Joshi, P. C. Weeraddana, M. Codreanu, and M. Latva-aho, "Weighted sum-rate maximization for MISO downlink cellular networks via branch and bound," *IEEE Trans. Signal Process.*, vol. 60, no. 4, pp. 2090–2095, Apr. 2012.

Fan Liu (S'16) received the Bachelor's degree in information engineering and the Ph.D. degree in electronics science and technology from Beijing Institute of Technology, Beijing, China, in 2013 and 2018, respectively. From 2016 to 2018, he was with the Communications and Information Systems research group, Department of Electrical and Electronic Engineering, University College London, London, U.K., as a visiting student. His research interests include precoding designs for MIMO systems, signal detection and estimation, and convex optimization. He received the Marie Curie Individual Fellowship in 2018, and has been recognized as an Exemplary Reviewer for the IEEE TRANSACTIONS ON COMMUNICATIONS.

Longfei Zhou (S'14) received the B.S. degree from Beijing Institute of Technology, Beijing, China, in 2013 and the Ph.D. degree from Peking University, Beijing, China, in 2018, all in electronics engineering. His research interests include signal processing designs and optimization techniques for wireless communication. He was the recipient of the Best Paper Award from the IEEE WCSP 2016.

Christos Masouros (M'06–SM'14) received the Diploma degree in electrical and computer engineering from the University of Patras, Patra, Greece, in 2004, and the M.Sc. by research and Ph.D. in electrical and electronic engineering from the University of Manchester, Manchester, U.K., in 2006 and 2009, respectively. In 2008, he was a Research Intern with the Philips Research Laboratories, U.K. From 2009 to 2010, he was a Research Associate with the University of Manchester and from 2010 to 2012, a Research Fellow with Queens University Belfast. He has held a Royal Academy of Engineering Research Fellowship from 2011 to 2016.

He is currently an Associate Professor with the Communications and Information Systems Research Group, Department of Electrical and Electronic Engineering, University College London, London, U.K. His research interests lie in the field of wireless communications and signal processing with particular focus on green communications, large scale antenna systems, cognitive radio, interference mitigation techniques for MIMO, and multicarrier communications. He was the recipient of the Best Paper Award in the IEEE GLOBECOM Conference 2015, and has been recognized as an Exemplary Editor for the IEEE COMMUNICATIONS LETTERS, and as an Exemplary Reviewer for the IEEE TRANSACTIONS ON COMMUNICATIONS. He is an Editor for the IEEE TRANSACTIONS ON COMMUNICATIONS, an Associate Editor for the IEEE COMMUNICATIONS LETTERS, and was a Guest Editor for the IEEE JOURNAL ON SELECTED TOPICS IN SIGNAL PROCESSING issues "Exploiting Interference towards Energy Efficient and Secure Wireless Communications" and "Hybrid Analog/Digital Signal Processing for Hardware-Efficient Large Scale Antenna Arrays."

Ang Li (S'14) received the Ph.D. degree in the Communications and Information Systems research group, Department of Electrical and Electronic Engineering, University College London, London, U.K., in 2018. He is currently a Postdoctoral Research Associate with the School of Electrical and Information Engineering, University of Sydney, Sydney, NSW, Australia. His research interests lie in the field of beamforming and signal processing techniques for MIMO systems.

Wu Luo (M'09) received the B.S., M.S., and Ph.D. degrees from Peking University, Beijing, China, in 1991, 1998, and 2006, respectively, all in electronics engineering. He is currently a Professor with the School of Electronics Engineering and Computer Science, Peking University. His research interests include wireless and satellite communication networks, channel estimation, interference cancellation and suppression, MIMO networks, and channel coding techniques. He was the recipient of Best Paper Award from IEEE WCSP 2016.

Athina Petropulu (F'08) received the Undergraduate degree from the National Technical University of Athens, Athens, Greece, and the M.Sc. and Ph.D. degrees from Northeastern University, Boston MA, USA, all in electrical and computer engineering. She is a Distinguished Professor with the Department of Electrical and Computer Engineering Rutgers University, the State University of New Jersey, NJ, Piscataway, USA having served as Chair of the department during 2010–2016. Before joining Rutgers in 2010, she was the faculty with Drexel University. She held Visiting Scholar appointments at SUPELEC, Universite' Paris Sud, Princeton University and University of Southern California.

Dr. Petropulu's research spans the area of statistical signal processing and wireless communications. She has made fundamental contributions in the area of cooperative approaches for wireless communications, physical layer security, MIMO radars using sparse sensing, and blind system identification using higher-order statistics. Her research has been funded by various government industry sponsors including the National Science Foundation, the Office of Naval research, the US Army, the National Institute of Health, the Whitaker Foundation, and Lockheed Martin and Raytheon.

Dr. Petropulu is the recipient of the 1995 Presidential Faculty Fellow Award given by NSF and the White House. She was an Editor-in-Chief of the IEEE TRANSACTIONS ON SIGNAL PROCESSING, the IEEE Signal Processing Society Vice President-Conferences and is currently member-at-large of the IEEE Signal Processing Board of Governors. She was the General Chair of the 2005 International Conference on Acoustics Speech and Signal Processing 2005, Philadelphia PA, and is General Cochair of the 2018 the IEEE International Workshop on Signal Processing Advances in Wireless Communications, (Kalamata, Greece. In 2005, she was the recipient of the IEEE Signal Processing Magazine Best Paper Award, and in 2012 the IEEE Signal Processing Society Meritorious Service Award for "exemplary service in technical leadership capacities." She is currently IEEE Distinguished Lecturer for the Signal Processing Society. In 2016, she was a President of the ECE Department Heads Association.